PHILCO Ford

WDL DIVISION
Philco-Ford Corporation
Palo Alto, California 94303

2 November 70

FREQUENCY SELECTIVE SURFACE SUBREFLECTOR DEVELOPMENT REPORT

Gary H. Schennum

Prepared by

Philco-Ford Corporation
WDL Division
Palo Alto, California

Prepared For

Massachusetts Institute of Technology
Lincoln Laboratory

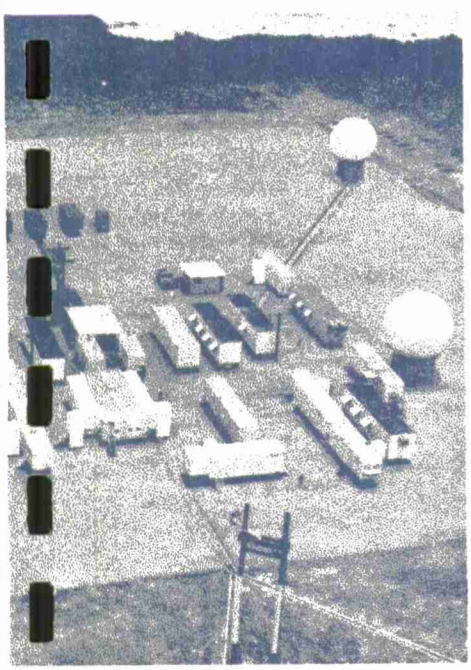

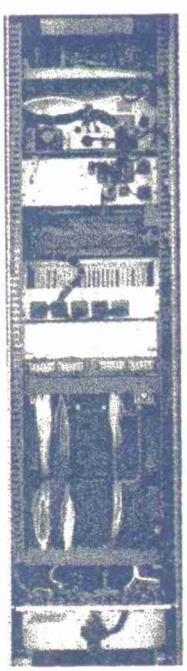

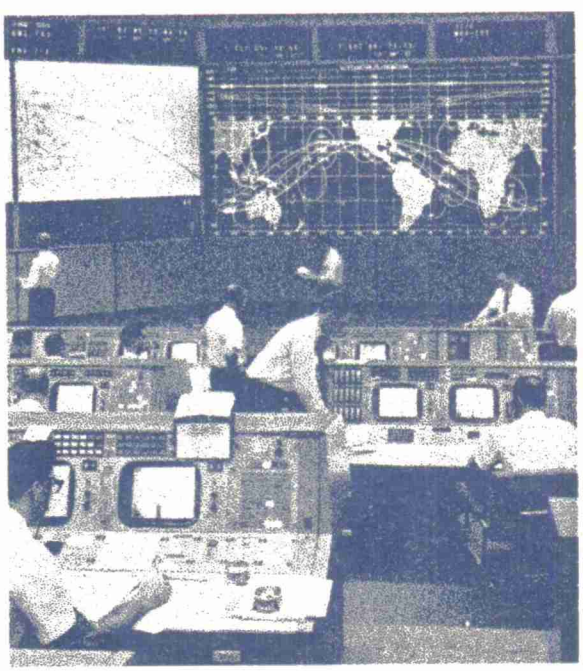

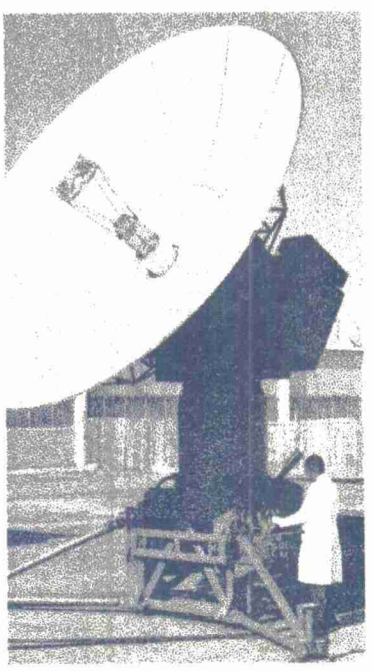

WDL-TR4327
2 November 70

FREQUENCY SELECTIVE SURFACE SUBREFLECTOR DEVELOPMENT REPORT

Gary H. Schennum

Prepared by

Philco-Ford Corporation
WDL Division
Palo Alto, California

Prepared For

Massachusetts Institute of Technology
Lincoln Laboratory

Under

Purchase Order No. A-5137
Prime Contract No. AF 19-(628)-5167

This Report Covers the Period

29 January 1969 to 30 May 1970

ABSTRACT

PHILCO-FORD WDL-TR4327
FREQUENCY SELECTIVE
SURFACE SUBREFLECTOR
DEVELOPMENT REPORT
(29 Jan 69 to 30 May 70)
2 Nov 70

UNCLASSIFIED
AF19-(628)-5167

47 Pages

This development report describes the Frequency Selective Surface Subreflector developed for the M.I.T. Lincoln Laboratory-Milestone Hill Field Station. Before specifically describing the M.I.T. -FSS reflector, general design information applicable to any FSS reflector is given in the early parts of the text. A later section, which is titled "Application in the Final Assembly", describes the M.I.T.-FSS in particular. Back-up data used in the M.I.T.-FSS design is given in the Appendices.

Accepted for the Air Force
Joseph R. Waterman, Lt. Col. USAF
Chief, Lincoln Laboratory Project Office

TABLE OF CONTENTS

LIST OF ILLUSTRATIONS

LIST OF ILLUSTRATIONS (Continued)

LIST OF TABLES

FOREWORD

This work was supported in part by M. I. T. Lincoln Laboratory, Lexington, Massachusetts, under their contract with the Office of the Chief of Research and Development, Department of the Army, Advanced Ballistic Missile Defense Agency and by the Philco-Ford Corporation, Palo Alto, California, under an Independent Research Development Program. This report was prepared in compiance with Purchase Order No. A-5137 under Prime Contract No. AF19-(628)-5167 and covers the period from 29 January 1969 to 30 May 1970.

INTRODUCTION

The need, in microwave tracking and radar systems for antennas with a dual-frequency capability, has necessitated the development of multi-frequency, multi-purpose antennas. It is the purpose of this report to describe one type of dual-frequency antenna that has been made operational. In particular, this antenna is the M.I.T. - Millstone Hill antenna described in Table 1.

TABLE 1 CHARACTERISTICS OF M.I.T. - MILLSTONE HILL ANTENNA

PARAMETER	PERFORMANCE
Subreflector Diameter	10 ft
Subreflector Weight (Crosses and Radome)	450 lbs
Ground Plane with Comparator and UHF Turnstiles weight	450 lbs
Triangular Support Structure weight	180 lbs
Diameter of Parabolic Dish	84 ft
f/D of Parabolic Dish	0.3
Cassegrainian Feed Frequency	L-Band 1275 to 1315 MHz
Prime-Focus Feed Frequency	UHF 395-405 MHz VHF 150 MHz
Estimated FSS Subreflector Reflectivity Loss to Cassegrainian Feed	0.2 dB
Estimated FSS Subreflector Transmissivity Loss to Prime-Focus Feeds	Negligible
Peak Radar Power Density at Subreflector Center	700 W/in^2
Average Radar Power Density at Subreflector Center	21 W/in^2

The salient component of this antenna is the Frequency Selective Surface (FSS) [1] , which can be used as either a hyperbolic subreflector or a flat reflector. An FSS reflector is an array of passive resonant elements which will ideally behave as a solid metal reflective surface over its resonant frequency band, but allow RF energy to pass through it at other frequencies. The length, width, and spacing of these resonant elements are determined by the requirements of the system. Most of the present applications require circular polarization, necessitating the use of circularly symmetrical elements such as cross-dipoles or rings. Because of the ease of fabricating dipoles and cross-dipoles and the simplicity of their analytical treatment, most of the experimental and theoretical work conducted by the authors and others [2] - [5] has been with dipoles or cross-dipoles.

A dual-purpose reflector can also be constructed of non-resonant elements such as metal discs or hexagons [6] . This type of reflector has the advantage of a large reflectivity bandwidth, with the disadvantage of a higher reflectivity loss over the transmission band when compared to a resonant-element structure.

According to Babinet's principle [7] , a dual of the FSS reflector could be achieved by using resonant slots rather than resonant elements. This type of FSS reflector would behave as a transparent surface over its resonant frequency band, but reflect RF energy at other frequencies. Because of this duality, much of the data and analysis presented in this report, although derived explicity for resonant cross-dipoles, can be applied to resonant slots.

Hyperbolic Subreflector Application

An FSS hyperbolic subreflector allows a feed, excited at the FSS resonant frequency, to be used in a Cassegrainian geometry, while a second feed, excited at another frequency, can be located behind the FSS to illuminate the main reflector in a prime-focus geometry. Figure 1 shows the Cassegrainian/prime-focus geometry of the FSS subreflector. In most applications it is advisable to use the high-frequency (f_H) feed as the Cassegrainian feed and the low-frequency (f_L) feed at the prime focus. With this type of feed arrangement the resonant elements of the FSS subreflector will be less than a half-wavelength at the frequency of the

prime-focus feed. For an FSS subreflector designed for the reverse feed

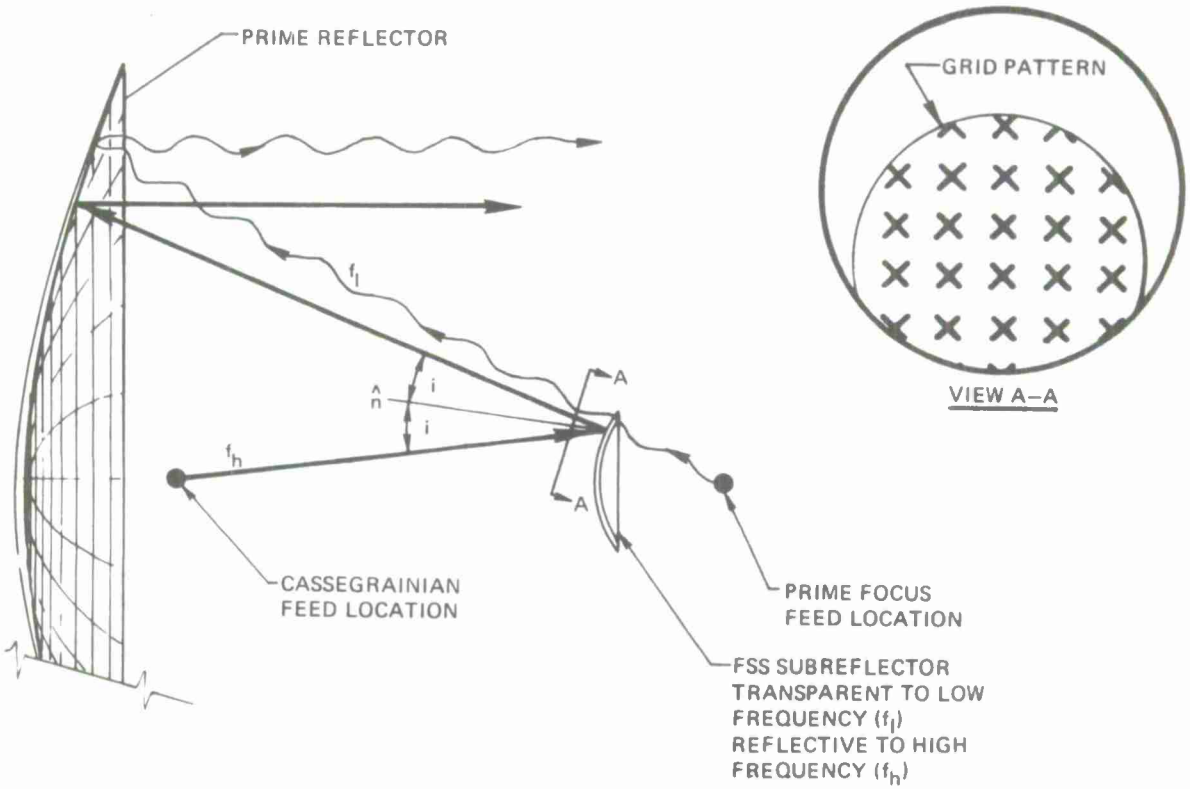

Figure 1 Prime-Focus/Cassegrainian Geometry

arrangement, the resonant elements would be greater than a half-wavelength in length at the prime-focus frequency; this could result in a significant distortion of the prime-focus feed pattern. The angle of incidence (i), which is determined by the incident ray (f_H), and the normal ($\hat{n}$) to the subreflector surface is an important design parameter of the FSS; that is, an FSS subreflector must be designed so that high reflectivity is obtained over the entire range of incident angles. For design purposes it is often convenient to simulate the subreflector as a series of FSS flat test panels and obtain design data from these panels over the range of incidence angles required of the subreflector. The data then obtained from the flat-panels can be used to obtain the efficiency of the FSS subreflector.

PERFORMANCE CRITERIA OF AN FSS REFLECTOR

The performance of an FSS reflector can be evaluated by a determination of the following properties:

- The reflectivity of the FSS reflector compared to a metal reference surface over the required reflectivity frequency band and the range of incidence angles.
- The transmissivity of the FSS reflector over the pass band.
- The power capability of the FSS reflector.

The above properties will be discussed initially in general terms and then specifically in regard to the high-power FSS subreflector developed for the M.I.T. Lincoln Laboratory-Millstone Hill radar site.

REFLECTIVITY

The element spacing, length, and width (as shown in Figure 2) are the design parameters that determine the reflectivity response of an FSS array. The reflectivity response has been measured by using the reflectivity test set-up shown schematically in Figure 3. By means of the sweep generator and pattern recorder, a reflected power versus frequency pattern is obtained. Two such patterns--one with the FSS in place, the other with the metal reference surface in place--are recorded on the same chart. The difference between the two patterns is then the measured reflectivity loss in dB of the FSS panel. Typical reflectivity patterns are shown in Figure 4. Figure 4A shows a high-reflectivity band centered about 1.3 GHz. The reflectivity frequency bandwidth found in Figure 4A and discussed elsewhere within this text is defined as the difference in frequency between the -0.5 dB points divided by the frequency midway between these points. The pattern shown in Figure 4B, due to the increased angle of incidence (i), does not have a high reflectivity band.

Several FSS panels were tested in the above manner at various incidence angles and the following properties have been observed:

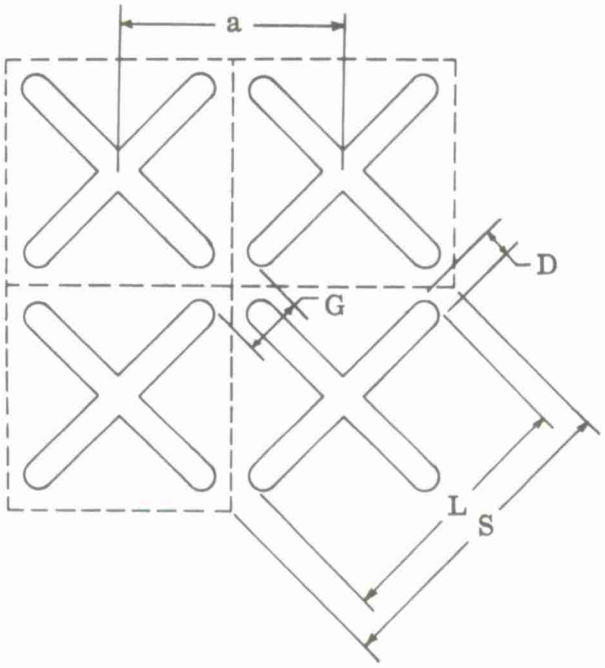

Figure 2 Array Geometry

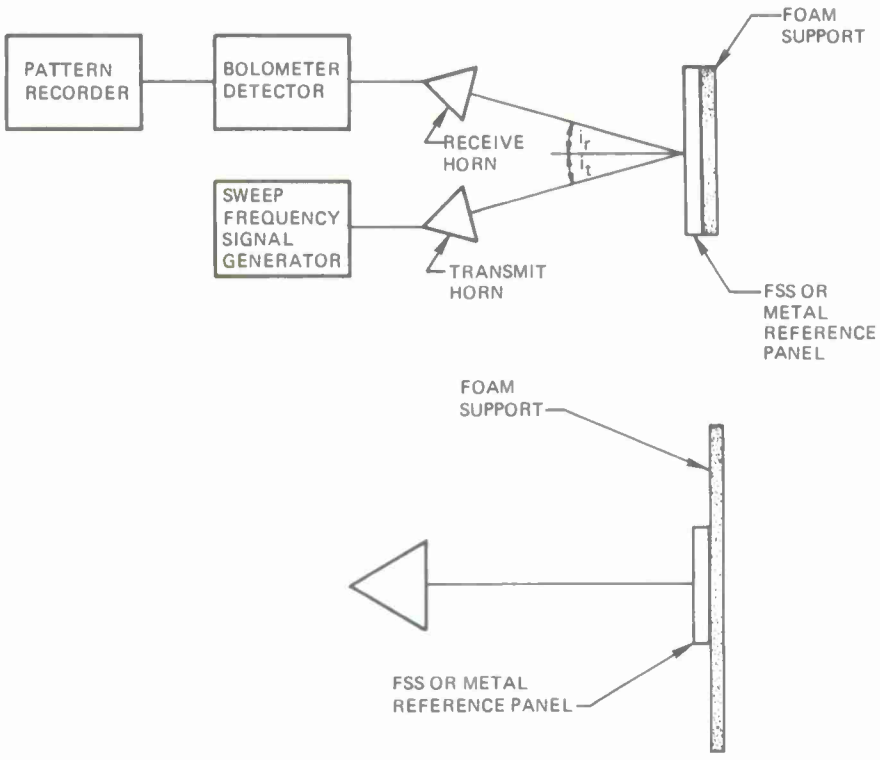

Figure 3 Reflectivity Test Set-Up

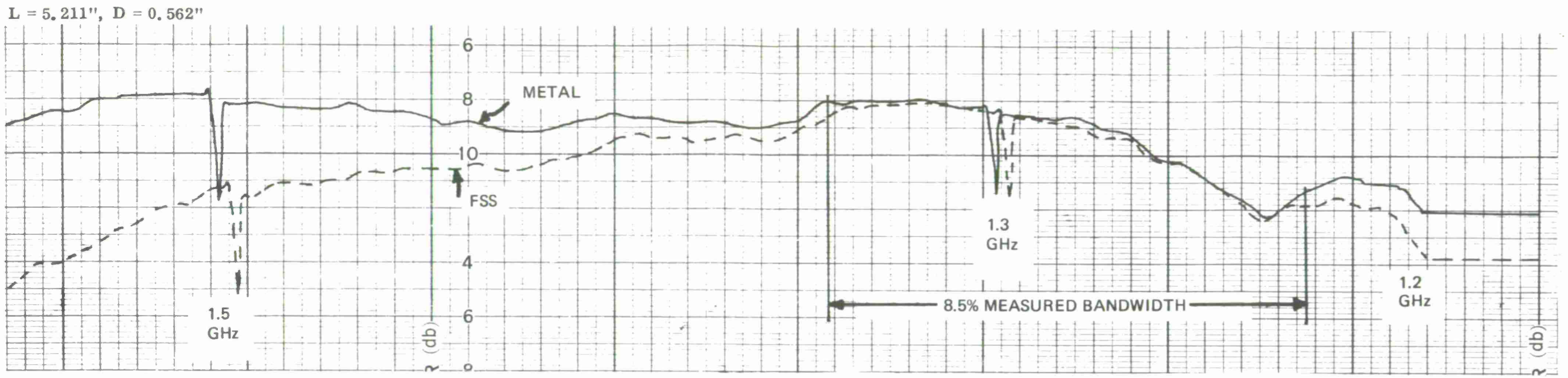

Figure 4A G/L = 0.5, Angle of Incidence (i) = 25°, Circular Polarization

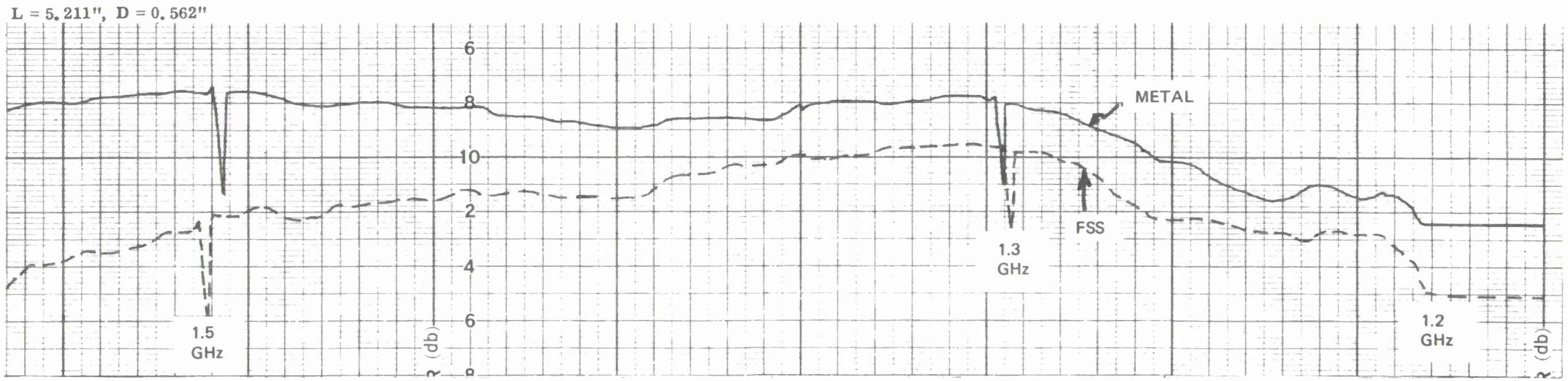

Figure 4B G/L = 0.5, Angle of Incidence (i) = 45°, Circular Polarization

Figure 4 Typical Swept Frequency Reflectivity Patterns

- The reflectivity is sensitive to the polarization of a linear electric field, especially at high-incidence angles. The reflectivity for the case of the electric field in the plane of incidence decreases more rapidly with incident angle than the case of the electric field perpendicular to the plane of incidence. The plane of incidence is a plane normal to the FSS panel and contains the incident and reflected rays as shown in Figure 5.
- For materials with a low dielectric constant ($\epsilon_r < 1.1$) between the cross-dipoles, the dipole length was greater than a half-wavelength for all the panels tested. This implies an inductive self-impedance and, hence, a capacitive mutual-impedance at the dipole input.
- Arrays consisting of flat strips and round rods of the same length, width, and spacing gave similar reflection performance.
- Beyond a certain element spacing at a given angle of incidence, the reflectivity loss will be high (>0.5 dB) for all frequencies. This spacing is related to the appearance of grating lobes.
- The reflectivity frequency bandwidth decreases with increasing angle of incidence. The decrease in bandwidth is primarily at the high end of the reflectivity band, while the reflectivity at the low end of the band remains essentially constant. This means the center frequency of the reflectivity frequency band decreases for increasing angle of incidence.
- The reflectivity frequency bandwidth increases with decreasing element spacing. The increase is primarily at the high end of the reflectivity frequency band, while the reflectivity at the low end of band remains essentially constant. This means the center frequency of the reflectivity frequency band increases for decreasing element spacing. This property of increasing bandwidth by decreasing element spacing can be used to compensate for the decrease in bandwidth caused by increasing the angle of incidence.
- From the previous two observations, it can be concluded that the low frequency end of the reflectivity frequency band does not shift appreciably in frequency with element spacing or angle of incidence. Low-frequency performance is primarily a function of element length, element width, and dielectric constant of the material between the elements.

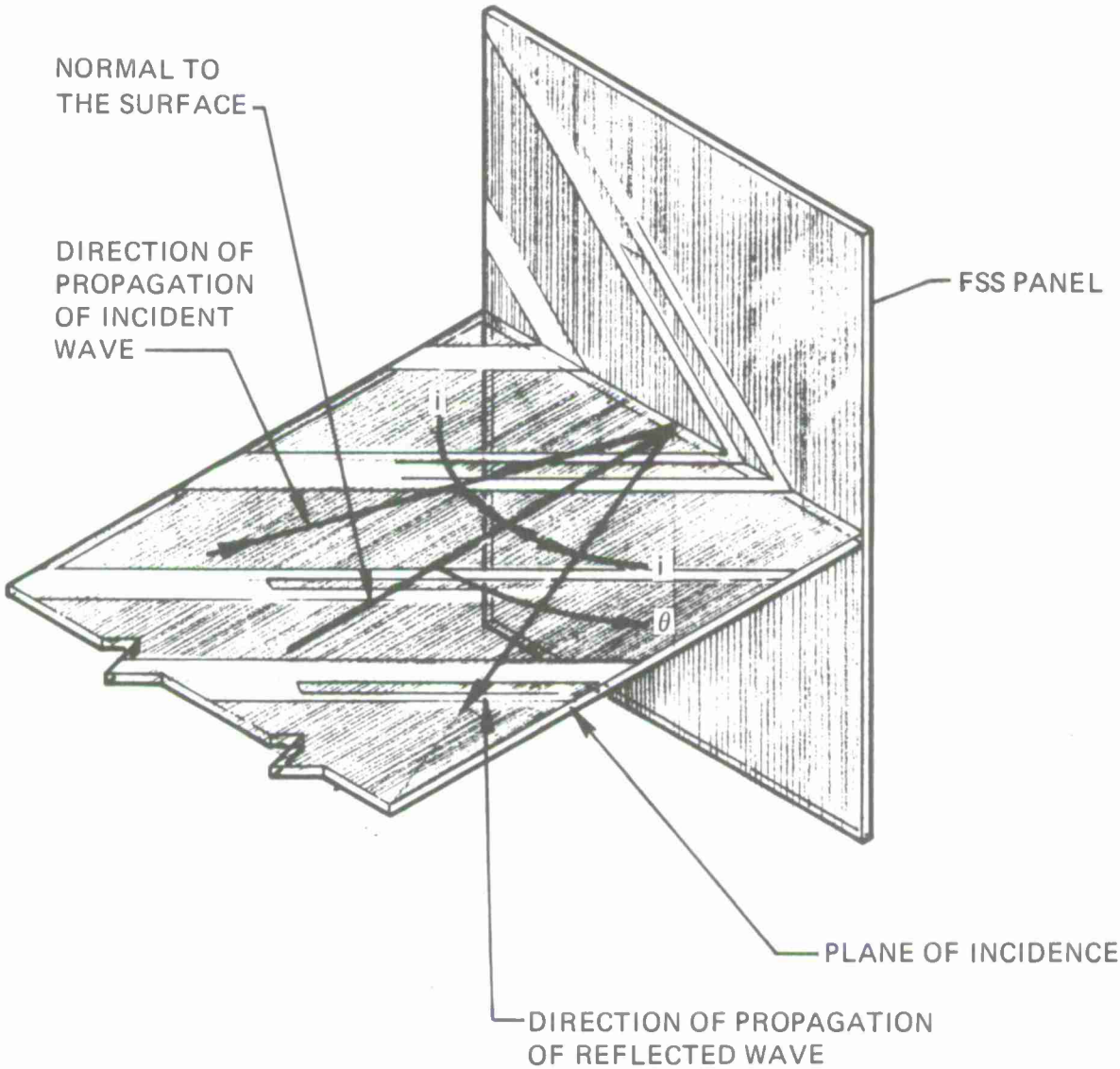

i = ANGLE OF INCIDENCE
= ANGLE OF REFLECTION
θ = ARBITRARY ANGLE IN THE
PLANE OF INCIDENCE
MEASURED FROM THE
SURFACE NORMAL

Figure 5 A Reflecting Panel

Bandwidth

To illustrate the effect of element spacing on bandwidth, a series of reflectivity tests were performed on the same elements at various spacings. It is convenient to express the array spacing in terms of the ratio of element gap to element length (G/L) for bandwidth comparisons. Arrays of G/L ratios of 0.15, 0.2, 0.35 and 0.5 were tested for reflectivity at several angles of incidence.

The variation of bandwidth with angle of incidence is shown in Figure 6 for the four G/L spacings specified above. In Figure 7 the bandwidth is plotted as a function of element spacing for incidence angles of 10°, 20°, 30°, 40° and 45°. It is interesting to note the decrease in bandwidth with increased incidence angle and increased element spacing.

Grating Lobes

When an array of radiators or scatterers are spaced in excess of a certain critical spacing, radiation or scattering will occur at angles other then the desired or specular direction. This spurious radiation or grating lobes represents a loss of energy and, hence, FSS reflectors should be designed so that grating lobes cannot occur.

It can be shown that grating lobes can exist for a broadside array whenever

$$(\pm n - a_\lambda \sin i) / a_\lambda \leq 1 \qquad (1)$$

where a_λ is the spacing between the elements in terms of wavelengths, i is the angle of incidence, and n is an integer $\neq 0$. Shown in Figure 8 is a plot of a_λ versus i for (1) = 1 with n = 1. The angles at which grating lobes can occur are given by

$$\theta = \mathrm{Cos}^{-1}\left[(\pm n - a_\lambda \sin i) / a_\lambda\right] \qquad (2)$$

where θ is defined in Figure 5.

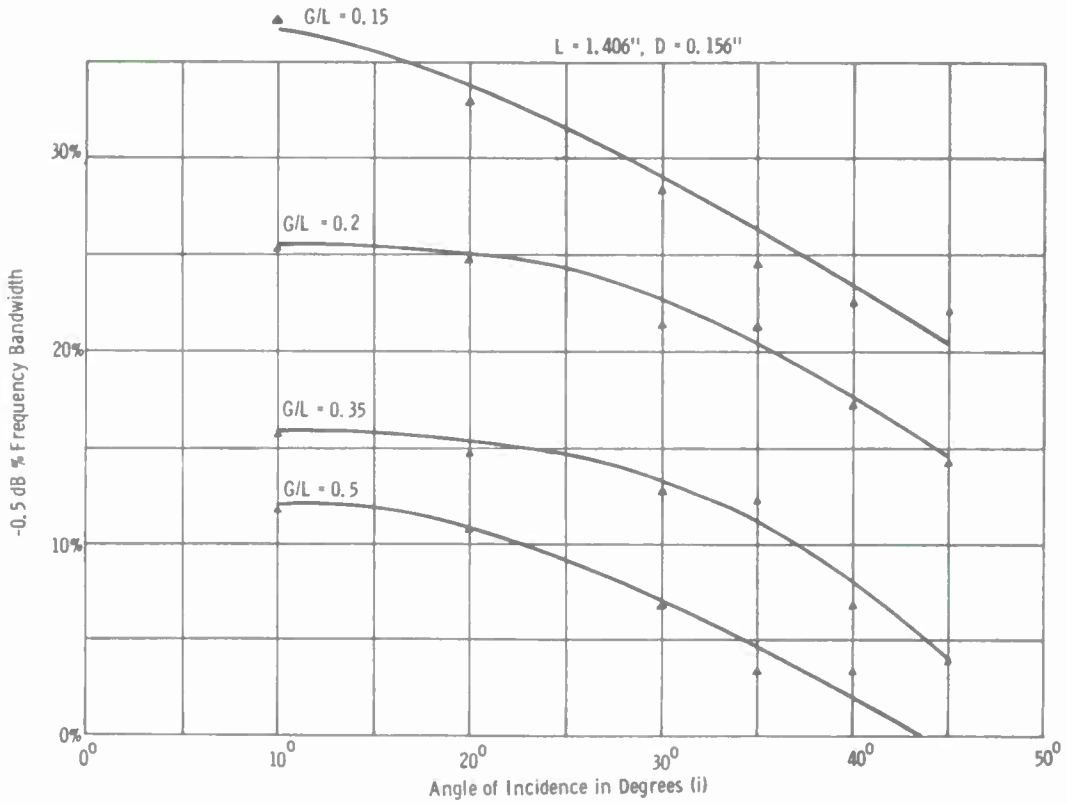

Figure 6 Bandwidth vs Angle of Incidence (i)

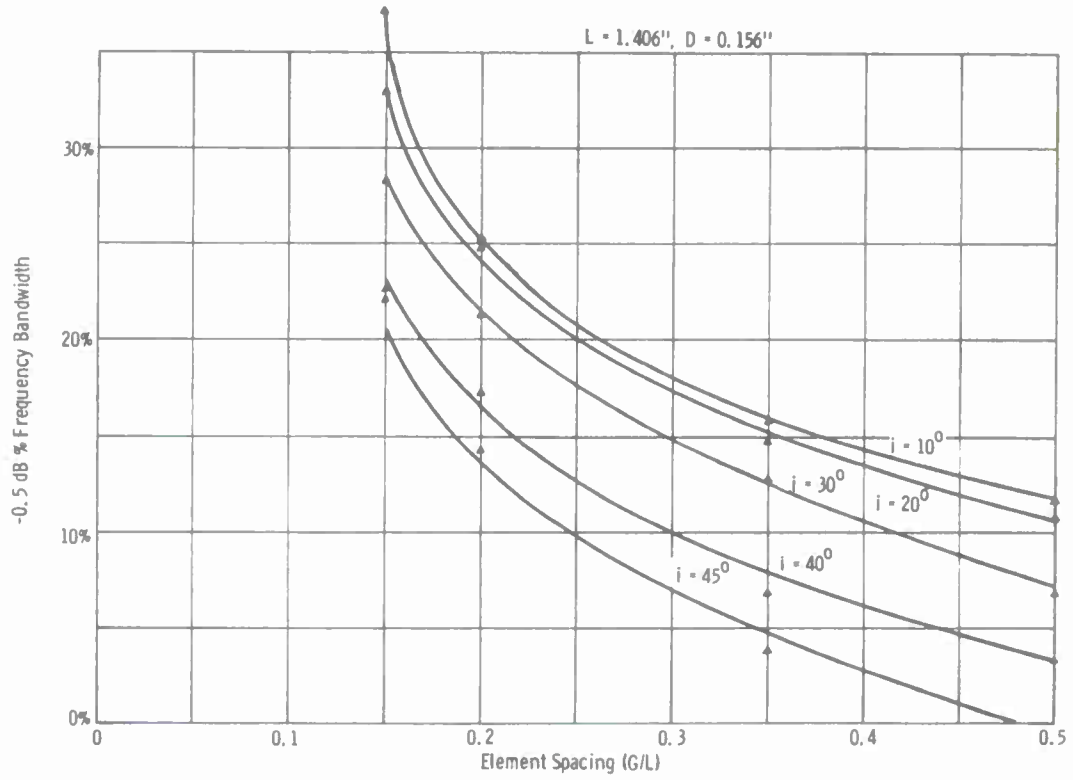

Figure 7 Bandwidth vs Element Spacing (G/L)

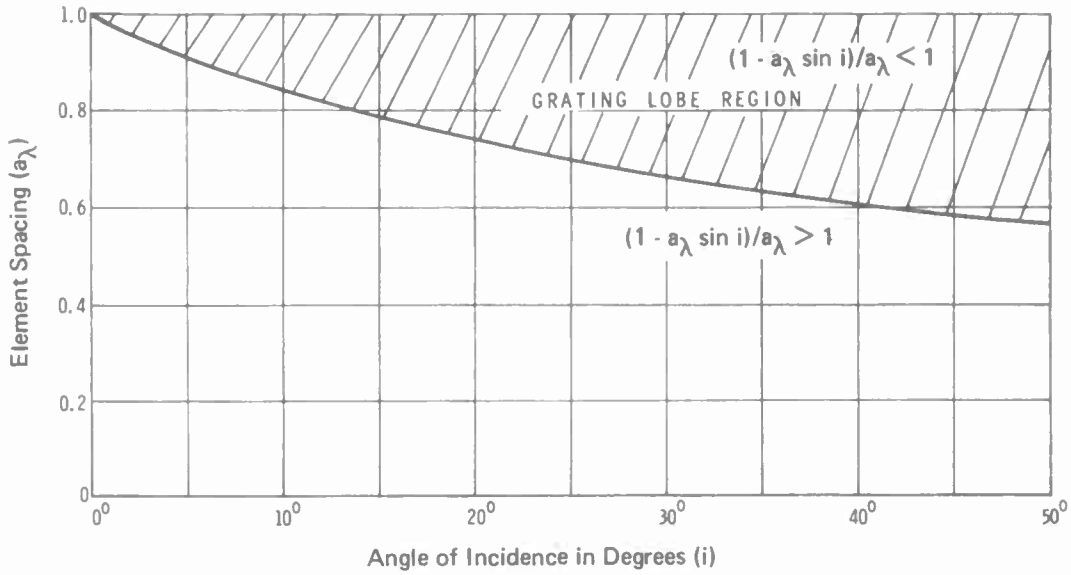

Figure 8 Grating Lobe Spacing vs Angle of Incidence (i)

A scatter pattern of a flat-panel operated in the grating lobe region is shown in Figure 9. The poor reflectivity can be directly attributed to the grating lobes which occur at the predicted angles.

To further emphasize the deleterious effects of grating lobes, the theoretical grating lobe loss is plotted in Figure 10 as a function of dipole spacing for a typical FSS hyperbolic subreflector. Essentially, the method of calculation is based on the principle that if the feed pattern is known, the reflector gain is calculable. The feed pattern was computed by a three dimensional summation of the individual dipole contributions. The dipoles were disposed on the hyperbolic surface with each dipole fed in phase and magnitude as if it were excited by a feed horn at the Cassegrain focus. A typical 12 dB aperture taper was assumed. To simplify the computer program certain assumptions were made which are crucial to the analysis. Principal among these are that the dipoles scatter as isotropic radiators and scatter independently. Nevertheless, it is believed that the results obtained represent in a qualitative way the effect of increasing dipole spacing on the FSS subreflector reflectivity.

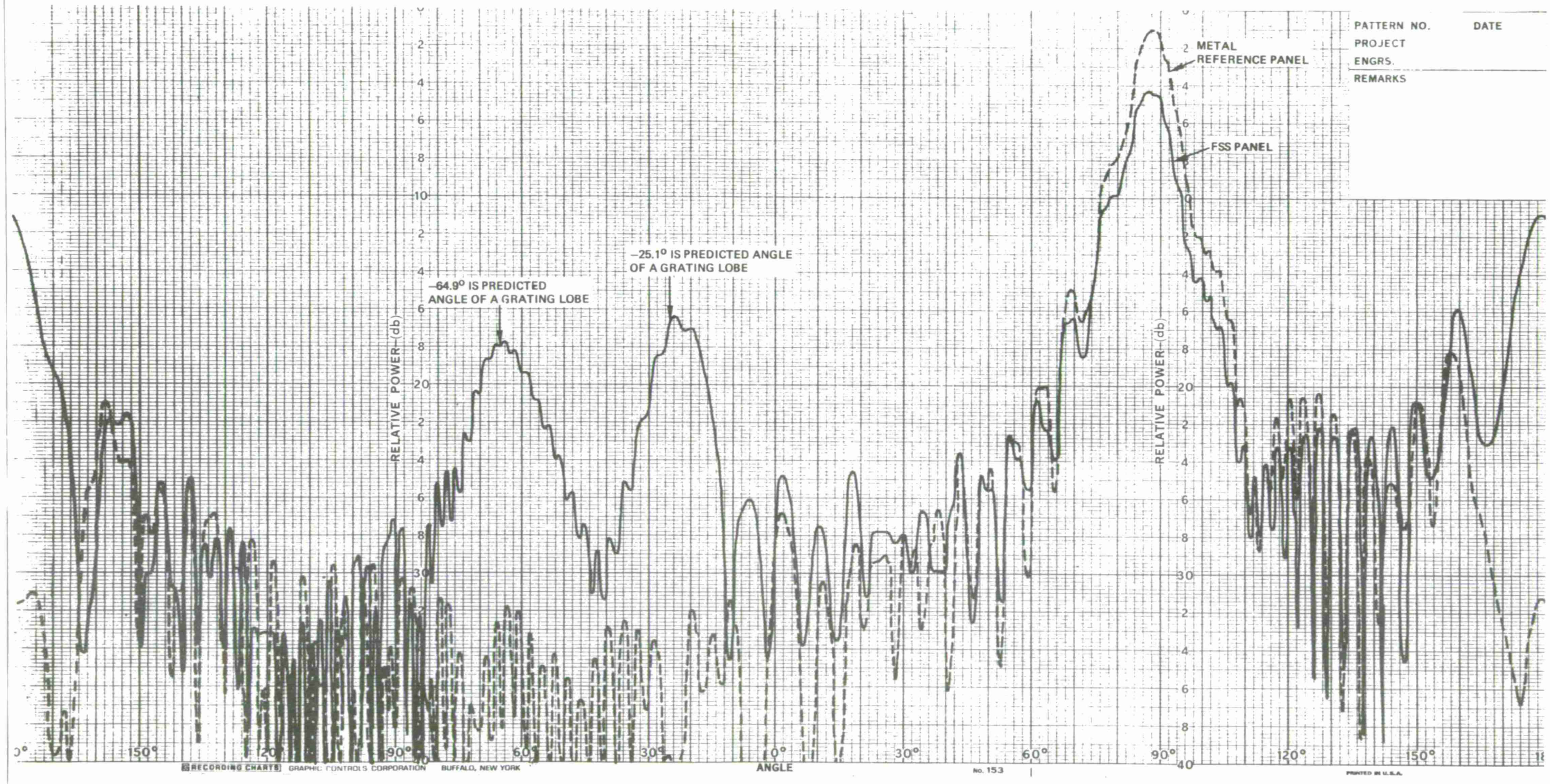

Figure 9 Flat-Panel Scatter Patterns, Circular Polarization Angle of Incidence (i) = 45°, L = 1.406", D = 0.156", and $a_\lambda = 0.606$.

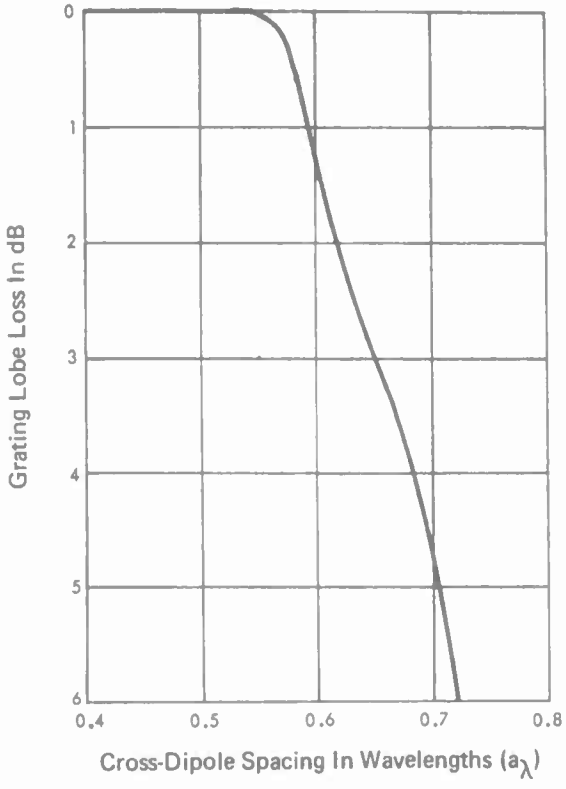

Figure 10 Grating Lobe Loss vs Cross-Dipole Spacing for a Typical Hyperbolic Reflector

TRANSMISSIVITY

An FSS subreflector will not be perfectly transparent to the energy emanating from the prime-focus feed. The non-perfect transparency is due to a portion of the incident energy being reflected by the elements of the FSS. The transparency primarily depends on the following factors:

- The ratio of the Cassegrainian feed frequency to the prime-focus feed frequency. The transparency will increase as this frequency ratio is increased.

- The reflectivity frequency bandwidth. For a fixed frequency ratio between the two feeds, the transmissivity over the pass band will increase if the reflectivity bandwidth is decreased. This seems reasonable as the reflectivity bandwidth can be decreased by decreasing the width of the resonant elements or by increasing the element spacing.

It is difficult to accurately predict the transmissivity of an FSS subreflector in a system by performing transmissivity measurements on flat-panels. This is due to the somewhat spurious or non-spectral reflection by the FSS on incident energy that is well away from the resonant frequency of the FSS dipole elements. For this reason, it is usually necessary to evaluate the transparency of the FSS in question by testing the prime-focus feed in the antenna feed subsystem or by scale model measurements.

HIGH POWER

Radar applications often require FSS subreflectors to operate at high-power levels. The potential problems at high-power levels are RF heating of the dielectric material of the FSS supporting structure and RF breakdown between the elements (arcing).

Dielectric Heating

When an FSS array of dipoles is illuminated with RF energy at high-power levels, and at the array resonant frequency, strong electric fields will be produced in the vicinity of the dipole tips. These electric fields can produce heating of the dielectric material, which could result in catastrophic failure. This problem can be particularly serious when the dipoles are embedded in the dielectric material. The degree of heating at resonance depends primarily on the following:

- The proximity of the cross tips to the dielectric material.
- The incident average power density.
- The dielectric constant and loss tangent of the dielectric material.
- The array resonant frequency (the theoretical loss increases linearly with frequency).
- The geometry of the dipole tips (size and shape).

When the average power density exceeds the capability of the embedding dielectric material, it becomes necessary to mount the cross-dipole elements in air on dielectric standoffs which make contact at the center of the cross-elements. This type of arrangement is termed an air-suspended FSS throughout this report. A photograph of such an array is shown in Figure 11.

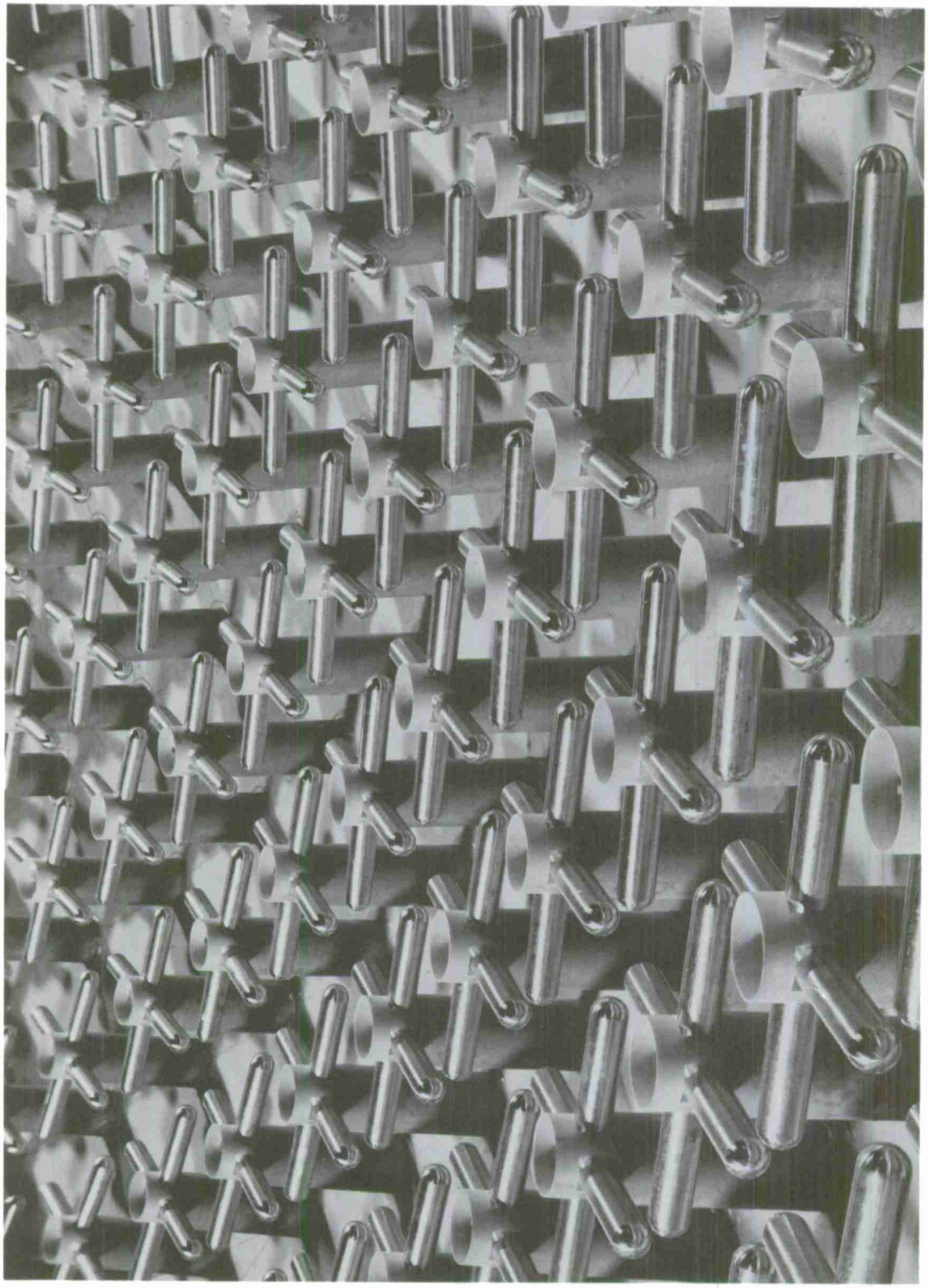

Figure 11 High Power Array

Arcing

If the peak incident power is high enough, RF breakdown between the tips of the cross-elements becomes a possible problem area. For the case of air-suspended cross-dipoles with hemispherical ends, an approximate solution for power capability has been derived. This derivation idealizes the RF breakdown mechanism to that of the static breakdown between two spheres. The dipole model used in the analysis is shown in Figure 12.

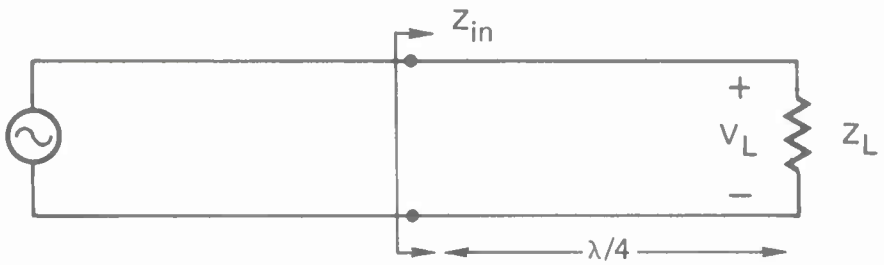

Figure 12 Dipole Model

Let P_R = the peak radar power (average radar power/duty factor) received per dipole

Z_{in} = the dipole impedance referred to the dipole input

Z_o = the average characteristic impedance of the dipole

$= 120 \left[\ln (L/a) - 1\right]$ - (Schelkunoff and Fries) [8]

where L = length of dipole

a = radius of dipole

$\bar{V}_L$ = the rms dipole tip-to-tip voltage difference

V_L = the peak dipole tip-to-tip voltage difference

Z_L = the dipole impedance referred to the tips

$Y_L = \frac{1}{Z_L}$ = the dipole admittance referred to the dipole tips

Then $$P_R = \mathrm{Re}\left\{ \bar{V}_L^{\,2} \quad Y_L \right\} \tag{3}$$

$$Z_L = \frac{Z_o^{\,2}}{Z_{in}} \quad \text{or} \quad Y_L = \frac{Z_{in}}{Z_o^{\,2}} \tag{4}$$

$$\mathrm{Re}\left\{Y_L\right\} = \frac{R_{in}}{Z_o^{\,2}} \tag{5}$$

$$P_R = \bar{V}_L^{\,2} \frac{R_{in}}{Z_o^{\,2}} = V_L^{\,2} \frac{R_{in}}{2Z_o^{\,2}} \tag{6}$$

It can be shown that the peak dc electric field between two spheres is given by

$$E = 0.9 \frac{r+G/2}{rG} V_L \tag{7}$$

where r = radius of spheres
G = gap spacing between spheres
V_L = potential difference between spheres

The two gaps where breakdown can occur are shown in Figure 13 as G_1 and G_2. The orientations of the incident electric fields which can excite the two gaps are also shown in Figure 13.

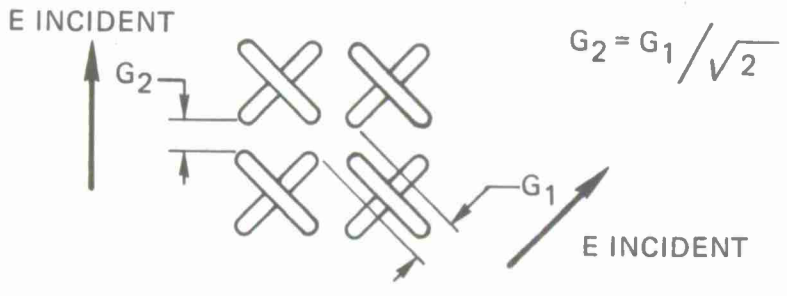

Figure 13 Gap and Electric Field Configuration

Let the voltage induced across gap $G_1 = V_L$, then the voltage induced across gap $G_2 = V_L/\sqrt{2}$, because the exciting incident field is titled 45 degrees to the dipole arms.

From (7), the electric fields induced across gaps G_1 and G_2 are then respectively

$$E = 0.9 \frac{r+G_1/2}{rG_1} V_L, \text{ across gap } G_1 \tag{8a}$$

$$E = 0.9 \frac{r+G_2/2}{rG_2} \frac{V_L}{\sqrt{2}} = 0.9 \frac{r+G_1/(2\sqrt{2})}{rG_1} V_L, \text{ across gap } G_2 \tag{8b}$$

From (8a) and (8b), the electric field across gap G_1 is greater than across G_2; hence, arcing should occur across G_1 before G_2. The assumption is now made that the dc voltages and fields of (8a) and (8b) apply to time varying fields. This assumption allows (6) to be combined with (8a) and with (8b). By combining (6) with (8a), and (6) with (8b), and by letting $G_1 = G$, we have

$$P_R = 0.62 \frac{(rGE)^2 R_{in}}{(r+G/2)^2 Z_o^2}, \text{ for } G_1 \tag{9a}$$

$$P_R = 0.62 \frac{(rGE)^2 R_{in}}{(r+G/2\sqrt{2})^2 Z_o^2}, \text{ for } G_1 \tag{9b}$$

The power received by a cross is given by

$$P_R = S_R A \quad \text{where } S_R = \text{peak radar power density at cross} \quad \text{and } A = \text{collecting area of cross} \tag{10}$$

The area can be expressed as

$$A = (L+G)^2/2 \tag{11}$$

and the characteristic impedance as

$$Z_o = 120 \left[\ln (L/a) - 1\right] \tag{12}$$

Combining equations (9a) through (12), we have

$$S_R = 8.61 \times 10^{-5} \quad \frac{(rGE)^2 R_{in}}{(r+G/2)^2 (L+G)^2 (\ln (L/a) - 1)^2} \quad , \text{ for } G_1 \tag{13a}$$

$$S_R = 8.61 \times 10^{-5} \quad \frac{(rGE)^2 R_{in}}{(r+G/2\sqrt{2})^2 (L+G)^2 (\ln (L/a) - 1)^2} \quad , \text{ for } G_2 \tag{13b}$$

(13a) and (13b) can be used to calculate the approximate power capability of FSS arrays once the input resistance R_{in} and the maximum E field strength of air at the operating frequency are known. From equations derived by Munk [3], [4], a computer program has been written to calculate R_{in}. The dc dielectric strength of air (30 kV/cm) at standard temperature and pressure is a reasonable approximation to use for the maximum E field strength up to at least several gigahertz.

The most significant result of this calculation is that arcing does not appear to be critically related to the element spacing. This is apparent in Figure 26 where radar peak power density is plotted as a function of element spacing for a particular array discussed in a latter section of this text.

APPLICATION IN THE FINAL ASSEMBLY

Using the data derived from flat-panel testing, the first FSS subreflector with a high RF power capability was constructed and was placed into operation in May of 1970. This is a 10-foot FSS subreflector, designed and fabricated for the 84-foot dish at the M. I. T. Lincoln Laboratory-Millstone Hill radar site. The net radar peak power delivered to the Cassegrainian feed is 4.25 MW (125 kW average), from which it can be shown that the peak power density at the subreflector center is 700 W/in^2. The maximum average power density at the subreflector is 21 W/in^2 (15 pps. with a 2000 μsec pulse width, or a duty factor of 0.03). The FSS subreflector loss, compared to a metal subreflector, was required to be less than 0.5 dB at L-band (1275 to 1315 MHz), and essentially transparent at UHF (395 to 405 MHz).

From flat-panel test data and scale model range testing, it is estimated that the FSS subreflector reflectivity loss at L-band is about 0.2 dB with a high transparency to the UHF feed frequency. The reflectivity frequency bandwidth of the subreflector is estimated to be 15% from flat-panel testing (3% bandwidth required). Power tests on flat-panels indicate at least a 7 dB margin in RF power capability.

M.I.T. Subreflector Construction

A cut-away sketch of the subreflector is shown in Figure 14. The radome structure is a sandwich construction, consisting of two 0.040-inch resin-filled E-glass skins with a 0.75-inch polyurethane foam core. The cross-elements are supported by dielectric tubular standoffs that are bonded to the radome. The cross-elements were fabricated of 9/16-inch aluminum rod, which was cut to the design length and machined with hemispherical tips. These elements are notched at their centers and pressed together to give a "log cabin" type construction.

The radome is bonded to a dielectric spacer ring, which is, in turn, bonded to the UHF ground plane. The UHF ground plane provides the mount for the 4-element UHF turnstile array as well as providing the interface to the subreflector supporting structure. The ground plane is a box structure consisting of aluminum channel webs with dielectric facings. The ground plane was designed to be transparent at L-band and reflective at UHF frequencies. This was accomplished by placing a grid of aluminum strips on one of the dielectric facings.

An exterior view of the completed FSS subreflector is shown in Figure 15. The interior view that portrays the 489 tubular standoffs and cross-dipoles is shown in Figure 16. The FSS subreflector installed on the 84-foot Millstone dish is shown in Figure 17.

Grid Pattern of the M.I.T. Subreflector

The grid pattern for the placement of the crosses on the M.I.T. subreflector was tapered such that the spacing between the crosses varied from 0.56 λ_o at the radome center to 0.47 λ_o at the radome edge, where λ_o is the wavelength at

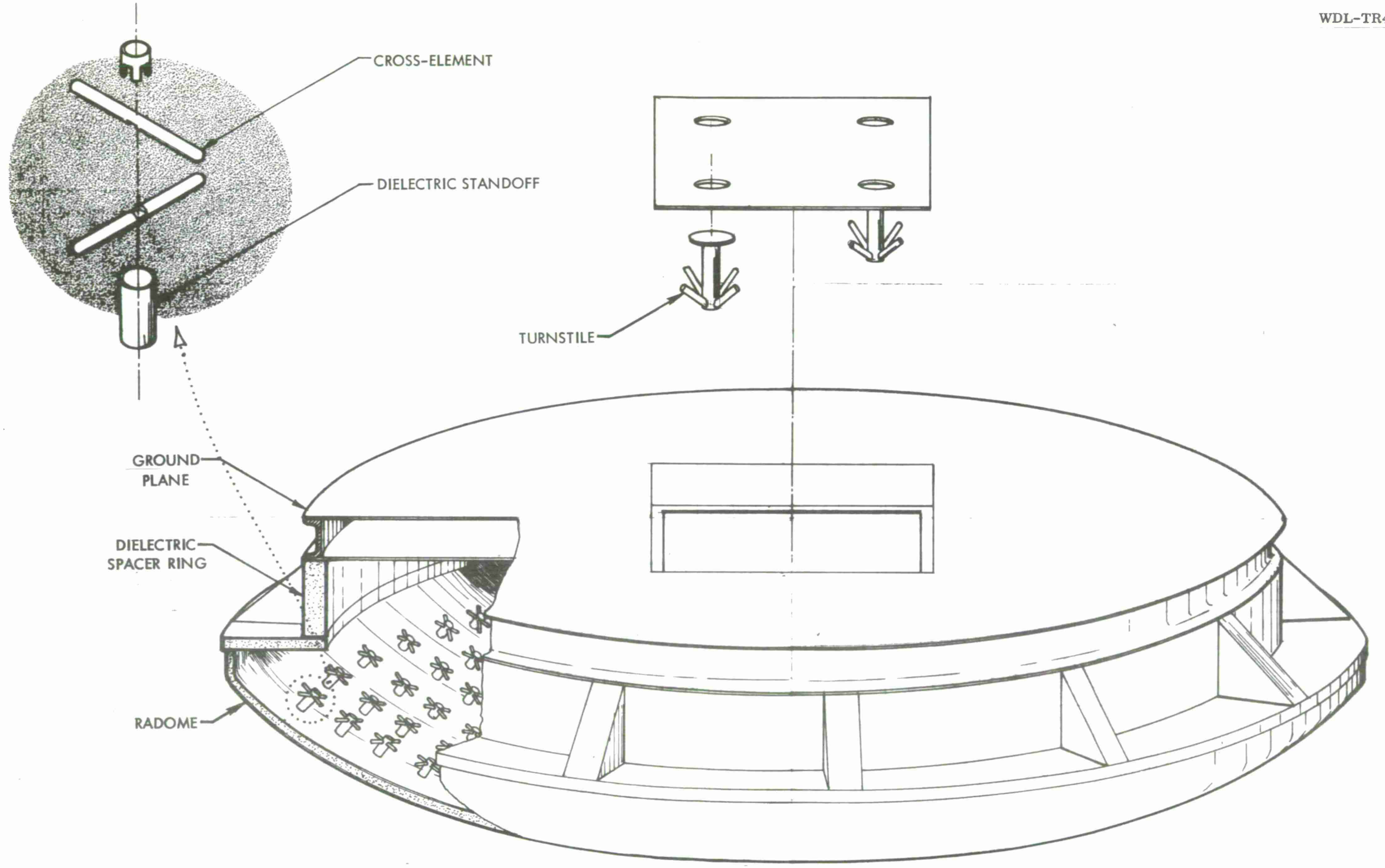

Figure 14 Cut-Away View of M.I.T. - FSS

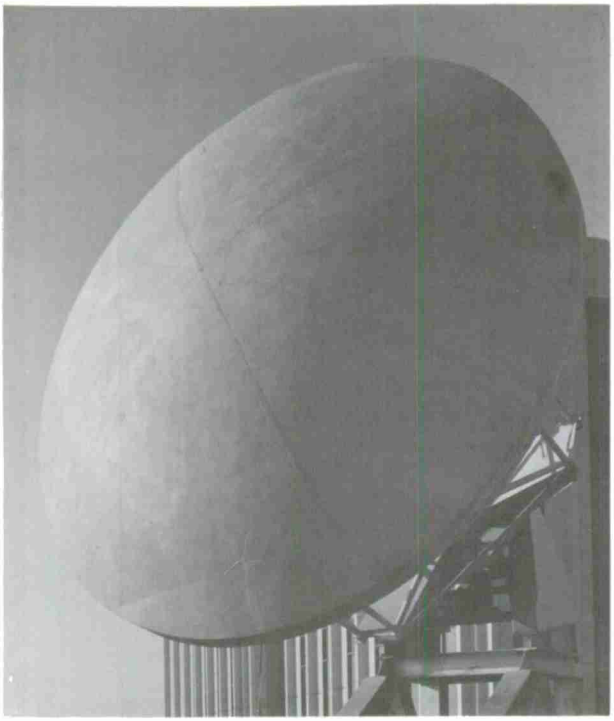

Figure 15 Exterior View of M.I.T. - FSS

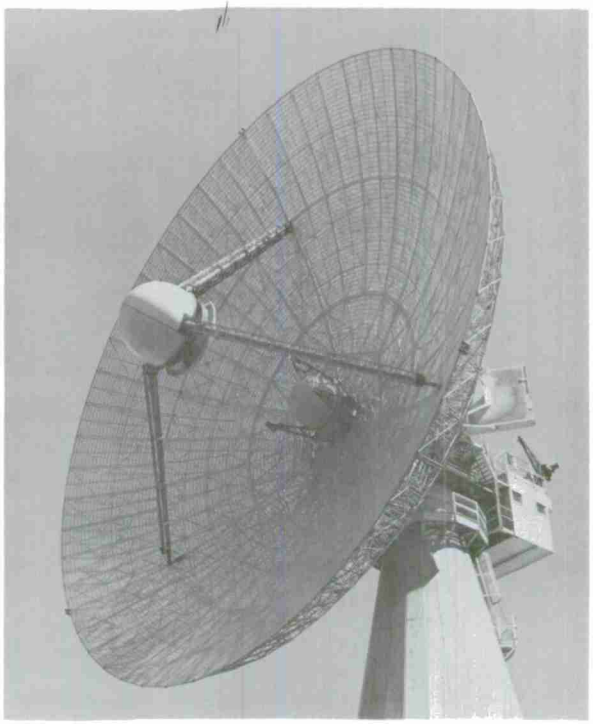

Figure 17 M.I.T. Millstone Hill Antenna with FSS Subreflector

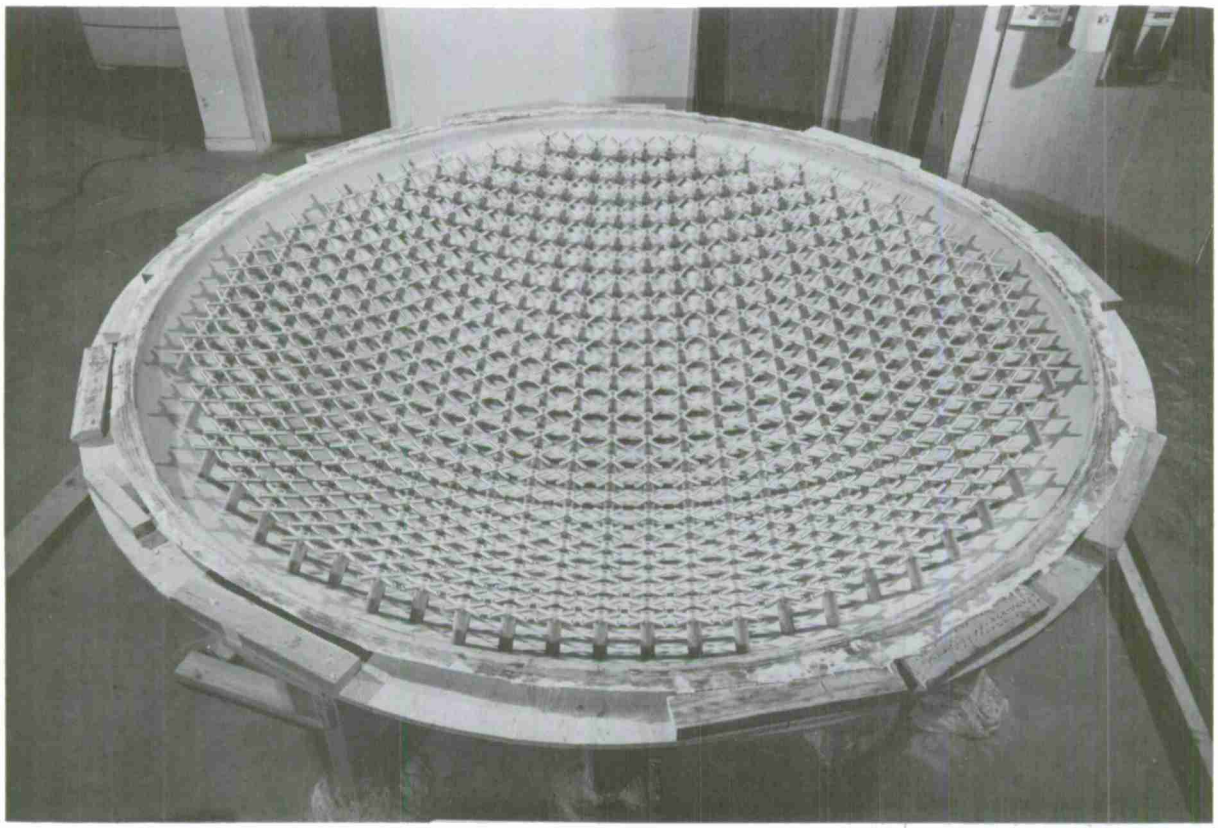

Figure 16 Completed Interior of M.I.T. - FSS

1295 MHz. From flat-panel reflectivity data, a higher cross density was required at the large incidence angles found near the radome edge. An element spacing of 0.47 λ_o proved sufficiently reflective to meet this requirement. A tapered grid pattern was used for the following reasons:

- For low angles of incidence, the reflectivity was found to be just as high for a 0.56 λ_o spacing as for a 0.47 λ_o spacing; therefore a tapered geometry would result in the fewest number of crosses, while maintaining high reflectivity.
- Wider spaced elements at the radome center results in a higher transmissivity to the UHF prime-focus feed.
- The squares of a tapered grid pattern map with less distortion onto the curvature of the radome than does a constant spaced grid pattern. This distortion which is illustrated in Figure 18 shows the dipole elements to be canted with respect to the diagonals of the distorted square.

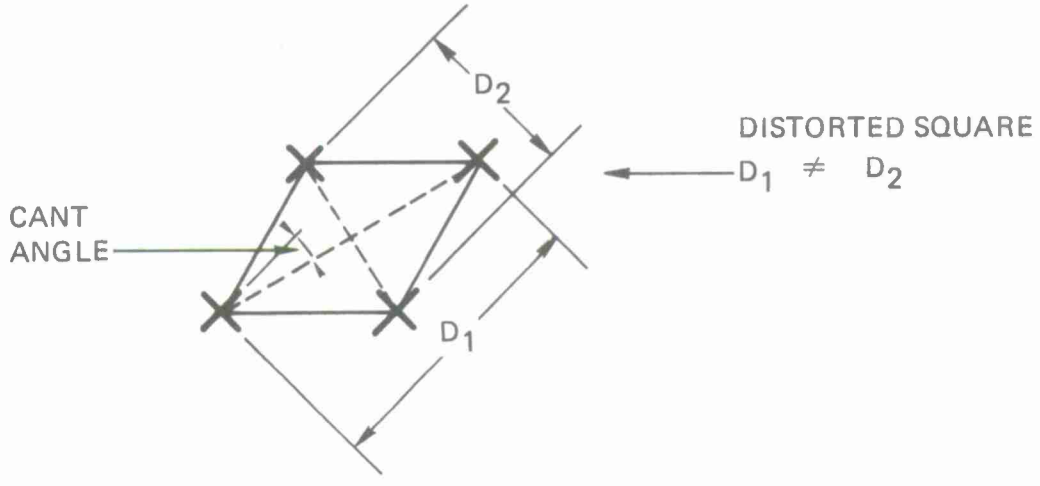

Figure 18 Effect of Distorted Grid

Scatter Patterns

Data on flat panels predicted a reflectivity loss of about 0.2 dB for the FSS subreflector over the required L-Band frequency range. To verify this reflectivity data and to investigate the effect of the FSS subreflector on the UHF prime-focus feed, a scale model of the M.I.T.-FSS subreflector was fabricated and tested.

Photographs of the scatter pattern test set-up are shown with the scaled FSS subreflector, and with a metal reference subreflector on the test fixture in Figures 19 and 20, respectively. The feed horn was fitted with a dielectric rod, adjustable in length, so that a 10 dB taper was achieved at the edge of the subreflector to simulate the M.I.T. subreflector feed. The principal and cross-polarized scatter patterns of the FSS subreflector, referenced to the solid subreflector, are shown in Figures 21A and 21B, respectively. As can be seen from the patterns, little difference exists between the FSS subreflector and the metal reference reflector.

The correspondence between the full scale FSS subreflector and the metal subreflector it replaced will probably not be as close as that indicated in Figure 21A. This is due to the full scale metal reflector being about a foot larger than the FSS subreflector. Also, the full scale FSS is preceded by a dielectric shell whose reflection coefficient is about 0.08.

In an attempt to obtain greater definition, the patterns 21A and 21B were expanded and evaluated. The evaluation consisted of taking data points at every peak and null of the scatter patterns and using these points in a computer integration program. Both principal and cross-polarized data were evaluated. Table 2 summarizes the percentage of energy in various angular intervals referenced to the total radiated power (principal plus cross).

TABLE 2 SCATTER PATTERN EVALUATION*

Polarization	Angular Interval	Metal Subreflector	FSS Subreflector
Principal C. P.	0°-80°	77.4%	77.5%
Cross C.P.	0°-80°	3.2%	2.9%
Principal C. P.	165°-180°	0.2%	0.2%
Cross C.P.	165°-180°	0.5%	0.7%
Cross C.P.	0°-180°	11.8%	11.9%

*Because of symmetry about the boresight axis, it was only necessary to evaluate one-half of the radiation pattern.

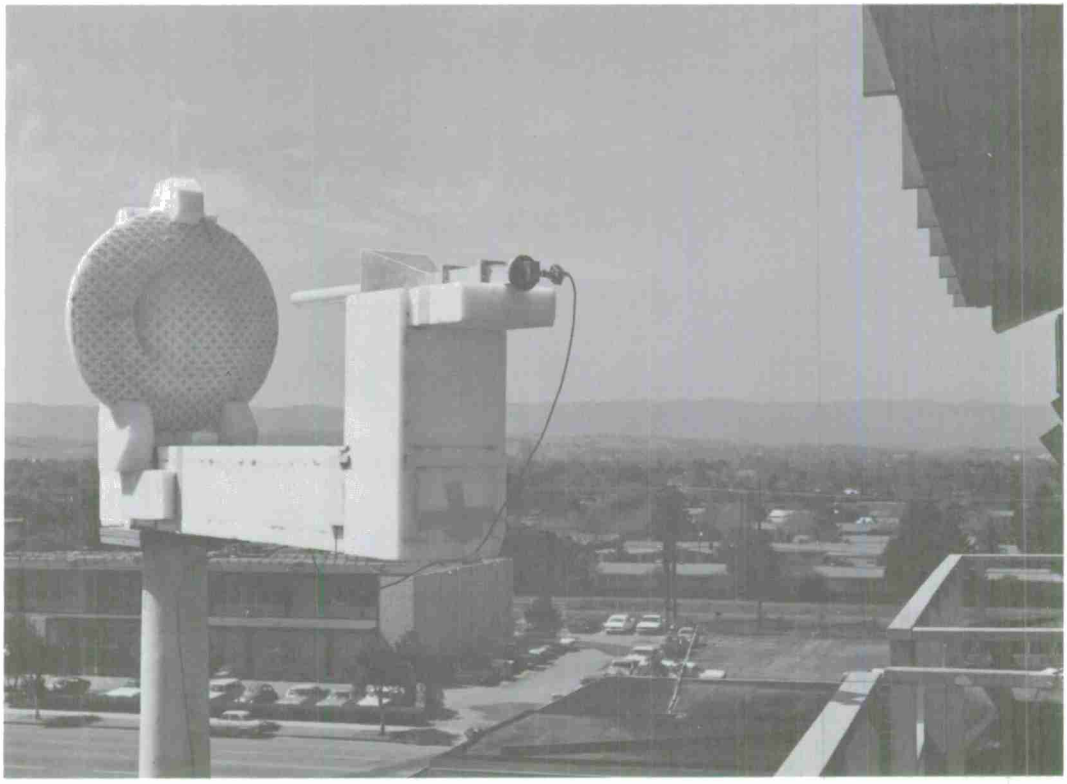

Figure 19 Scatter Pattern Test Set-Up with FSS Subreflector

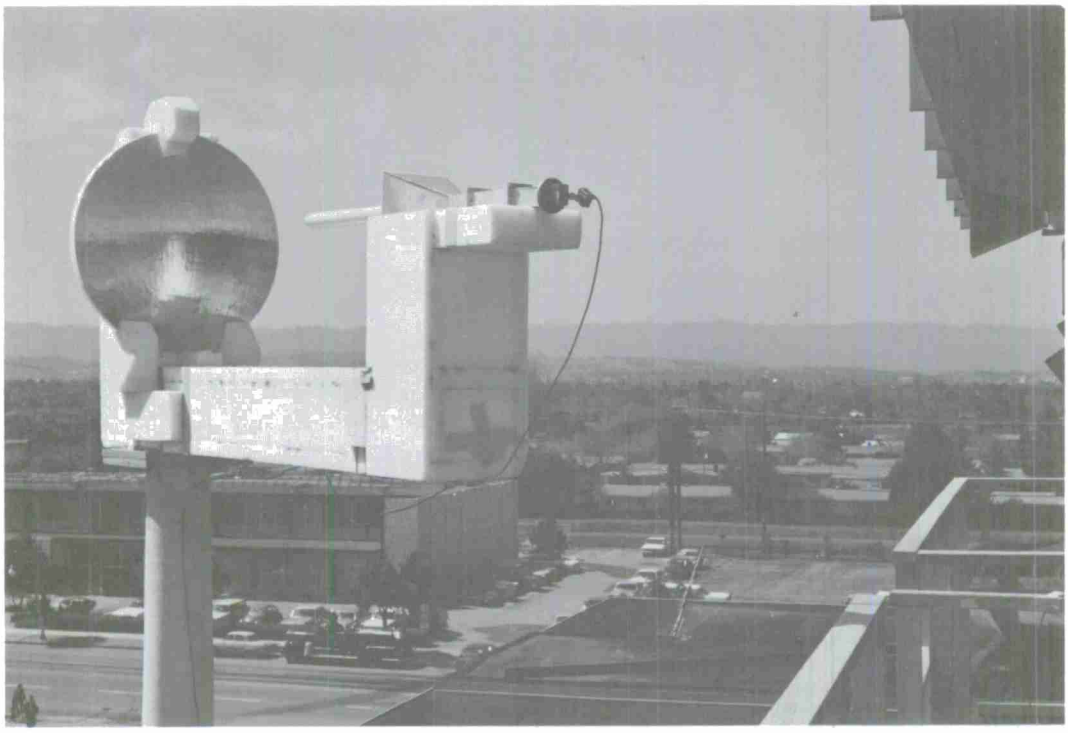

Figure 20 Scatter Pattern Test Set-Up with Metal Reference Subreflector

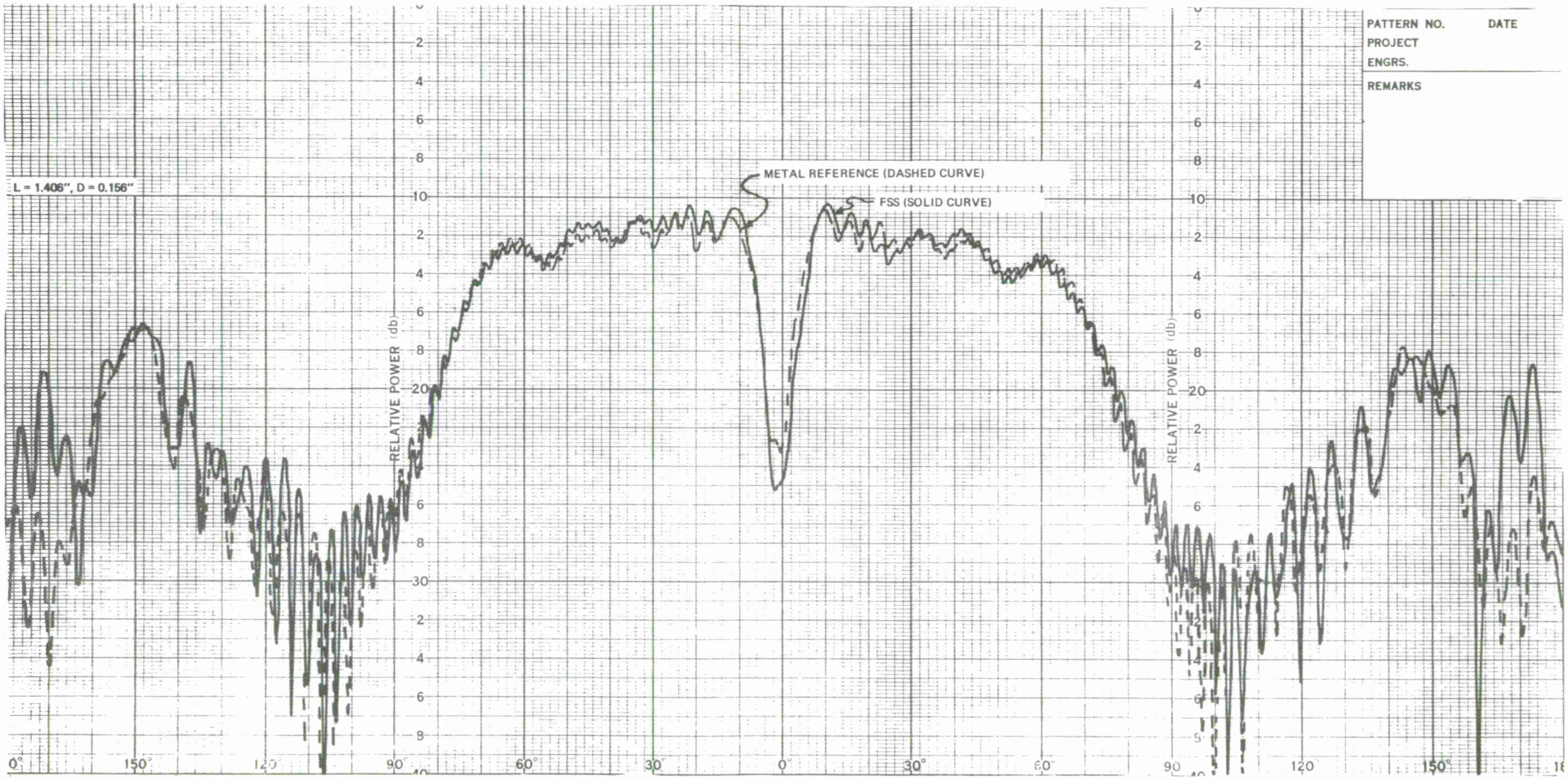

Figure 21A Scatter Pattern of Scaled M.I.T. Subreflector, Principal Circular Polarization, Frequency = 4.8 GHz.

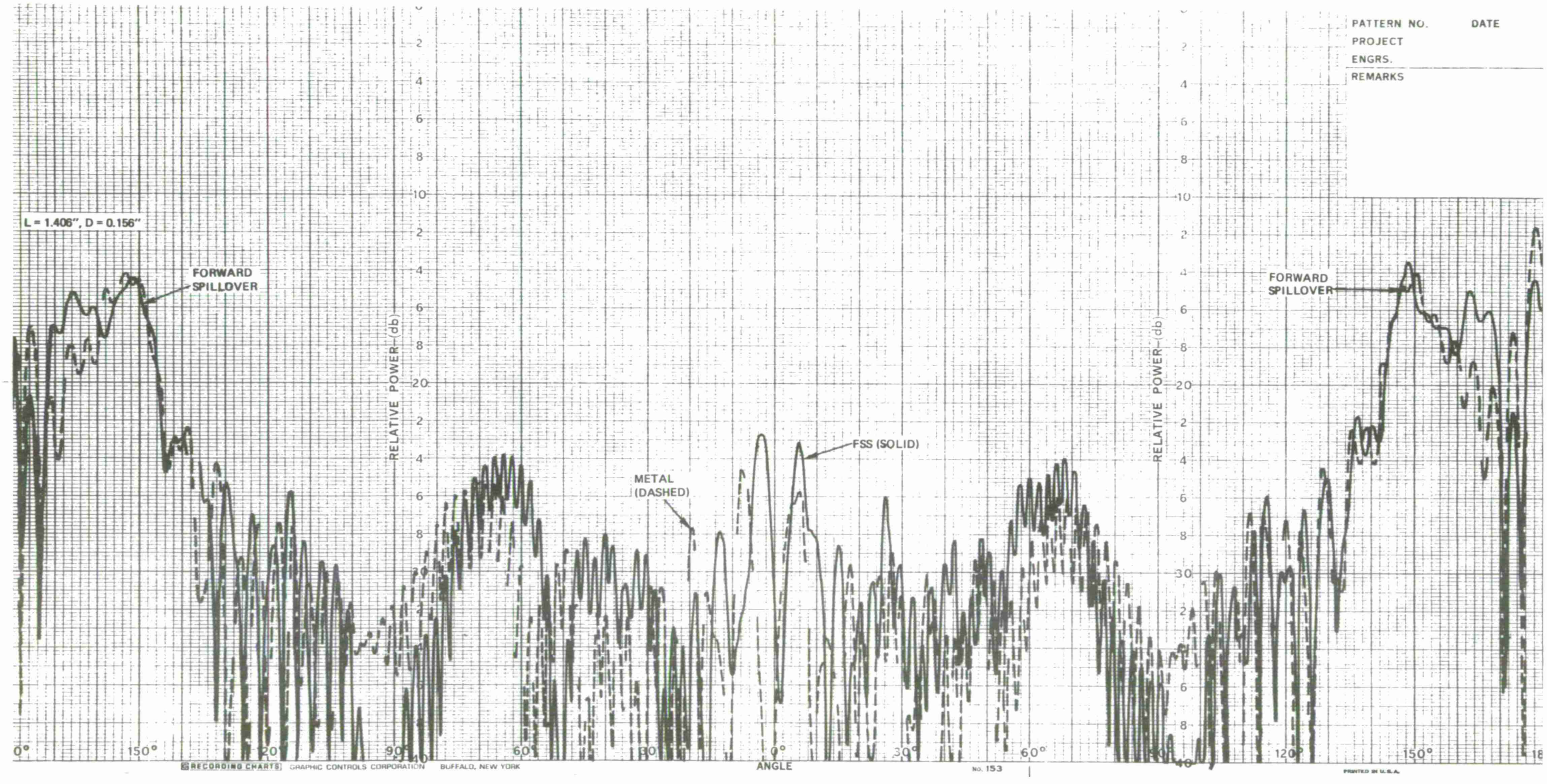

Figure 21B Scatter Pattern of Scaled M.I.T. Subreflector, Cross Circular Polarization, Frequency = 4.8 GHz.

From Table 2 it is apparent that the electrical differences at the Cassegrainian feed frequency between the FSS and metal subreflectors are quite small. The reflectivity loss from this data appears to be even less than the 0.2 dB predicted from flat-panel testing. To be conservative, however, the 0.2 dB value is taken to be the upper bound on the FSS reflectivity loss.

Transmissivity Patterns

Scaled UHF patterns and the turnstile VSWR were recorded with and without the scaled model FSS subreflector blocking a scaled feed to determine the transmissivity properties of the FSS subreflector. The actual full scale UHF feed consists of four turnstiles in a diamond pattern driven by a monopulse comparator, whereas only a single turnstile was used for scale model testing. For this reason the patterns of the scale model do not give a one-to-one correspondence with the full scale feed patterns. However, the qualitative effect of the FSS subreflector on the UHF feed can be determined by such patterns.

Two patterns were recorded—the first one with the feed turnstile mounted on a small ground plane is shown in Figure 22; the second pattern with the feed turnstile mounted on a scaled full-size ground plane is shown in Figure 23. The scaled UHF patterns were integrated for primary gain, forward spillover loss, and primary cross-polarization loss. The data is shown in Table 3.

TABLE 3

SCALED UHF-FEED PATTERN EVALUATION

	No FSS Small Ground Plane	FSS Present Small Ground Plane	No FSS Large Ground Plane	FSS Large Ground Plane
Gain	9.3 dB	9.12 dB	8.52 dB	7.91 dB
Cross-Polarized Loss	8.8%	16.6%	2.5%	4.0%
Forward Spillover	3.1%	3.8%	1.3%	1.2%
VSWR	1.17:1	1.19:1	1.23:1	1.28:1
On-Axis Axial Ratio	2.5 dB	2.5 dB	2.6 dB	2.5 dB

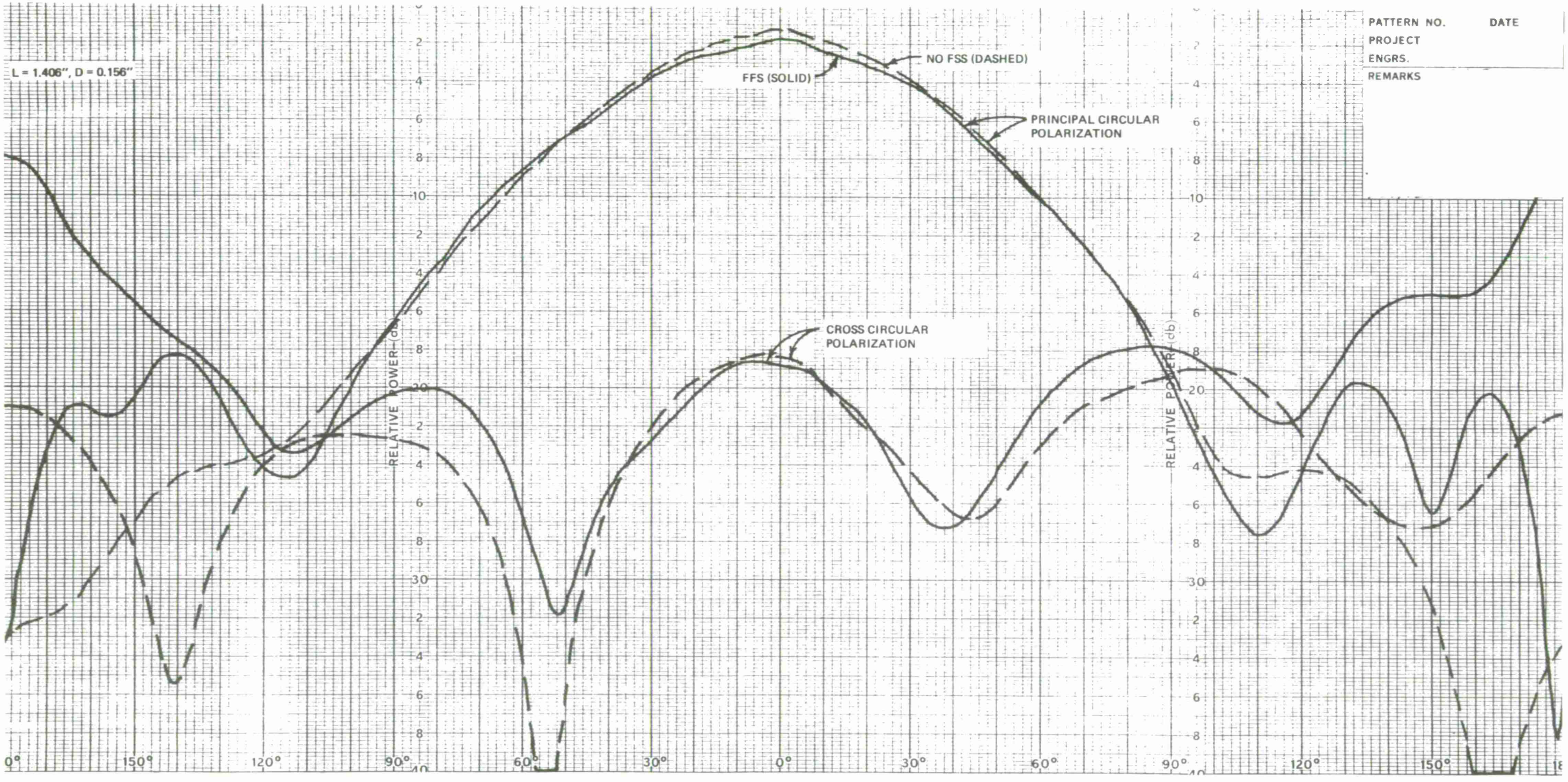

Figure 22 Scaled M.I.T.-FSS UHF Feed Patterns, Single Turnstile Mounted Over Small Ground Plane, Frequency = 1.482 GHz.

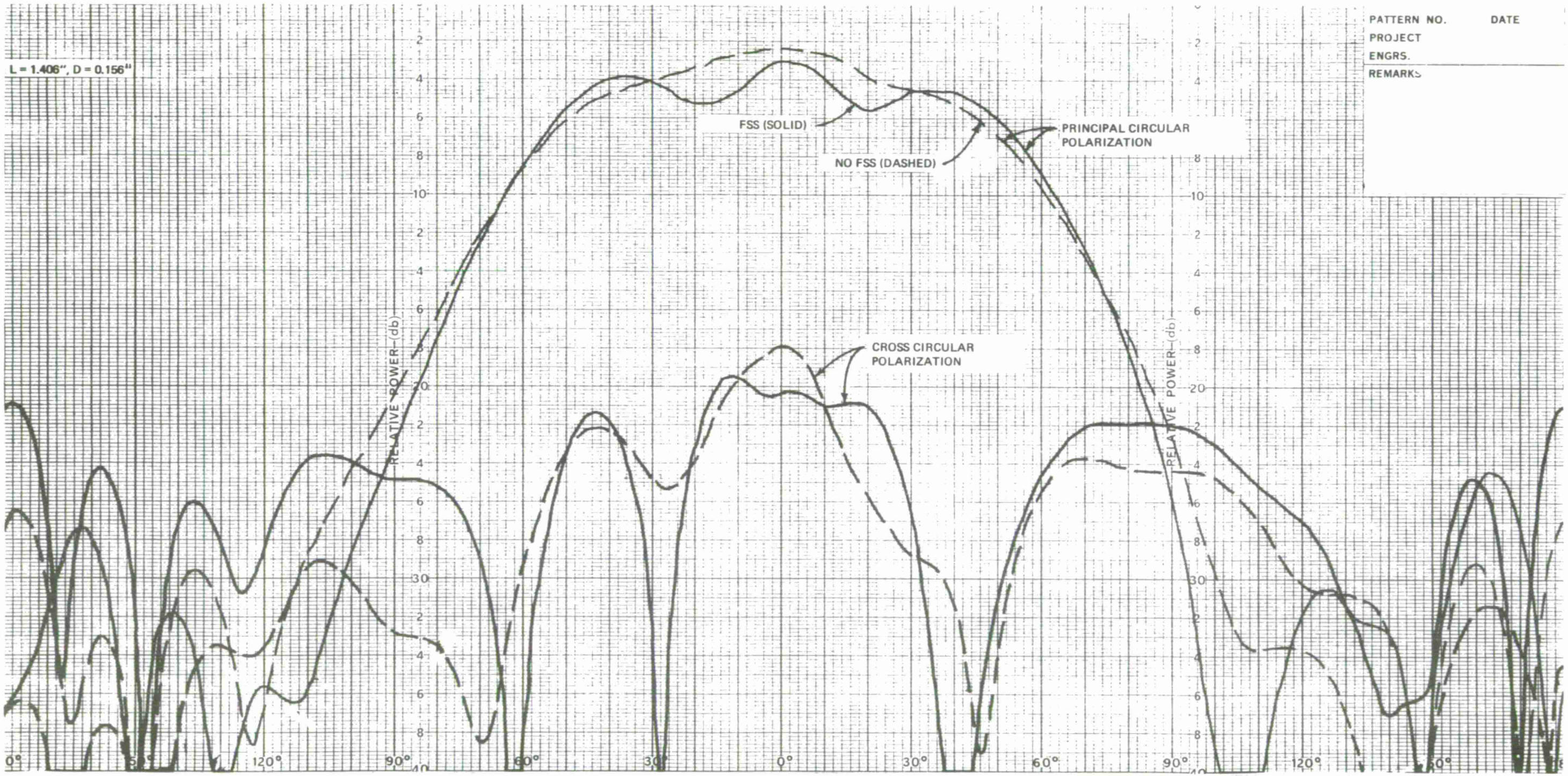

Figure 23 Scaled M.I.T.-FSS UHF Feed Patterns, Single Turnstile Mounted Over Large Ground Plane, Frequency = 1.482 GHz.

From the above data and the patterns, the following comments can be made:

- The increase in cross-polarized energy for the case of the small ground plane with and without the FSS present occurred primarily in the back direction. The data indicates that the FSS reflected approximately 8% of the incident energy in the back direction.
- The large ground plane decreased the cross-polarization loss greatly, so that this loss was about the same for "No FSS" as for the "FSS Present." This decrease occurs because the large ground plane re-reflects into the main beam the 8% of energy which was initially reflected by the FSS.
- The FSS subreflector and ground plane combination broadened the feed pattern. Since the 4-turnstile array to be used at M.I.T. has a pattern too narrow for the f/D = 0.3 dish, the broadened feed pattern will increase the secondary pattern gain if the phase error induced by the FSS and ground plane combination is not too severe. Also, the secondary difference pattern will probably be improved because of primary beam widening.
- The shallow peaks and nulls of Figure 23, which occur between ±50°, are due to the energy which is reflected by the FSS and then re-reflected by the large ground plane. This energy adds in-phase with the main beam at the peaks and out-of-phase at the nulls.
- The VSWR increase for the case of the "FSS Present" when compared to "No FSS" is negligible. Most of the reflected power, however, is probably absorbed by the terminated port of the turnstile hybrid, so that VSWR measurements are not too meaningful. This also applies to the full scale 4-element UHF array where most of the reflected energy will be absorbed by the orthogonal comparator port. Data was not taken for reflected energy at the orthogonal ports for either the full or 1/4 scale prime-focus feeds.

- The on-axis axial ratio which was derived from the turnstile antenna patterns of Figures 22 and 23 shows that the FSS has little if any effect on axial ratio. The actual axial ratio of the full scale turnstile array was measured to be 0.7 dB.

In addition to the UHF turnstiles, VHF loops (150 MHz) are simultaneously employed at the prime focus. Since the frequency factor spread between L-Band (1295 MHz) and VHF (150 MHz) is so large (>8), the FSS will be almost 100% transparent to the VHF feed frequency. The use of a triple frequency system and the ease of changing the prime-focus feeds is an important advantage of the FSS subreflector not obtainable any other way.

Power Capability of the M.I.T. Subreflector

The first attempt at developing a high power FSS test panel resulted in catastrophic failure at a power density of about 13 W/in^2 (60% of required value). A photograph of the panel during failure is shown in Figure 24. The panel is a sandwich construction consisting of two 0.040 inch resin-filled E-glass skins ($\epsilon_r = 4.0$, $\tan \delta = 0.01$) with a 0.75 inch polyurethane core ($\epsilon_r = 1.04$, $\tan \delta = 0.0005$). Thin aluminum crosses were then etched on one of the dielectric skins to form the completed FSS panel. The failure was due to the dipole electric fields causing excessive heating of the dielectric material. Once the dielectric deteriorated sufficiently, the array began to arc as evidenced in Figure 24.

Because of the dielectric heating, it was concluded that it would be necessary to air-suspend the cross-dipoles. In addition, the cross-dipole tip area was increased by making the dipoles of 9/16-inch diameter aluminum rod, with hemispherical ends. This increase in tip area increases the arcing threshold. The high-power tests on air-suspended cross-dipoles were initially conducted with the cross-dipoles supported by short standoffs (0.5 inch). At an average power density slightly above nominal (21 W/in^2), the surface temperature in a small region near the center of the test array had a measured temperature increase from an ambient of 18°F to 180°F. This temperature change was measured by using sensors which change color at some predetermined temperature. The dielectric heating indicated the presence of high localized electric fields. These

fields are the resultant of the incident electric field and the dipole fields. The dipole fields consist of the radiation term (1/r), the induction term ($1/r^2$), and the electrostatic term ($1/r^3$) found in the complete dipole-field expression. It has been shown by Ruze [9] that the power density at the innermost dielectric skin is at least 25 times greater than the incident field in localized areas for the case of the short standoffs. At a distance greater than $\lambda/4$ from the plane of the array, the induction and electrostatic terms essentially decay to zero so that the fields are similar to those of a wave reflected off a metal surface. It is well-known that when a uniform plane wave reflects off a good reflector at normal incidence, a standing wave exists with nulls occurring every half-wavelength.

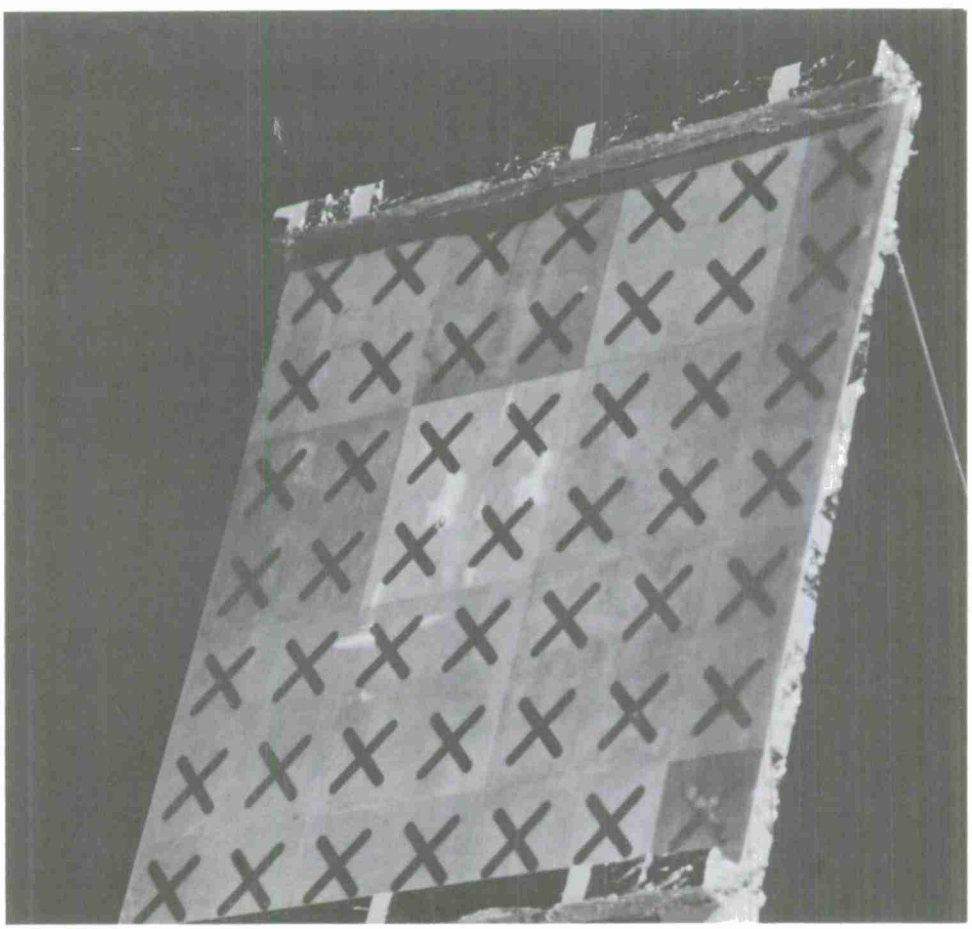

Figure 24 FSS Test Panel During RF Power Failure

For this reason, it was decided to use long standoffs, as shown in Figure 25, which would center the first null of the standing wave at the radome core center. Subsequent power tests up to 6 times the required 21 W/in^2 average power density verified low heating of the dielectric material.

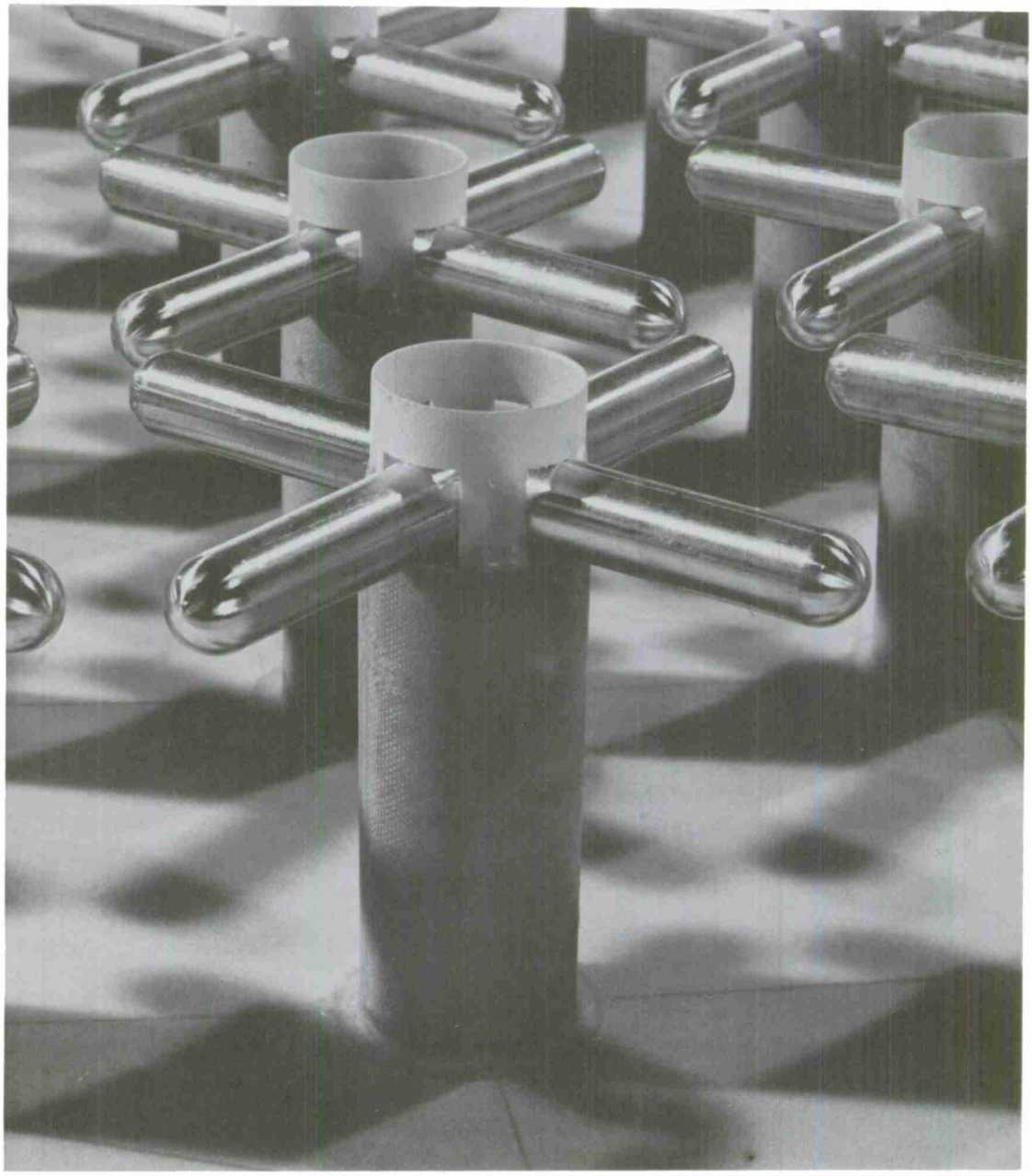

Figure 25 Cross-Dipole and Standoff Assembly

Plotted in Figure 26 is the theoretical, tested, and required peak radar power densities as a function of element spacing (G/L) for the elements used in the subreflector construction. The theoretical response was derived from (8a) where a dielectric strength of air of 30 kV/cm was assumed. The required power density is a function of element spacing (G/L) because the array cross-dipole density varies radially along the subreflector, and there is a 10 dB aperture taper across the subreflector. The high-power test range (shown in Figure 27) was limited to a peak radar power density capability of about 4 kW/in^2 (120 W/in^2 average) due to arcing in the waveguide run.

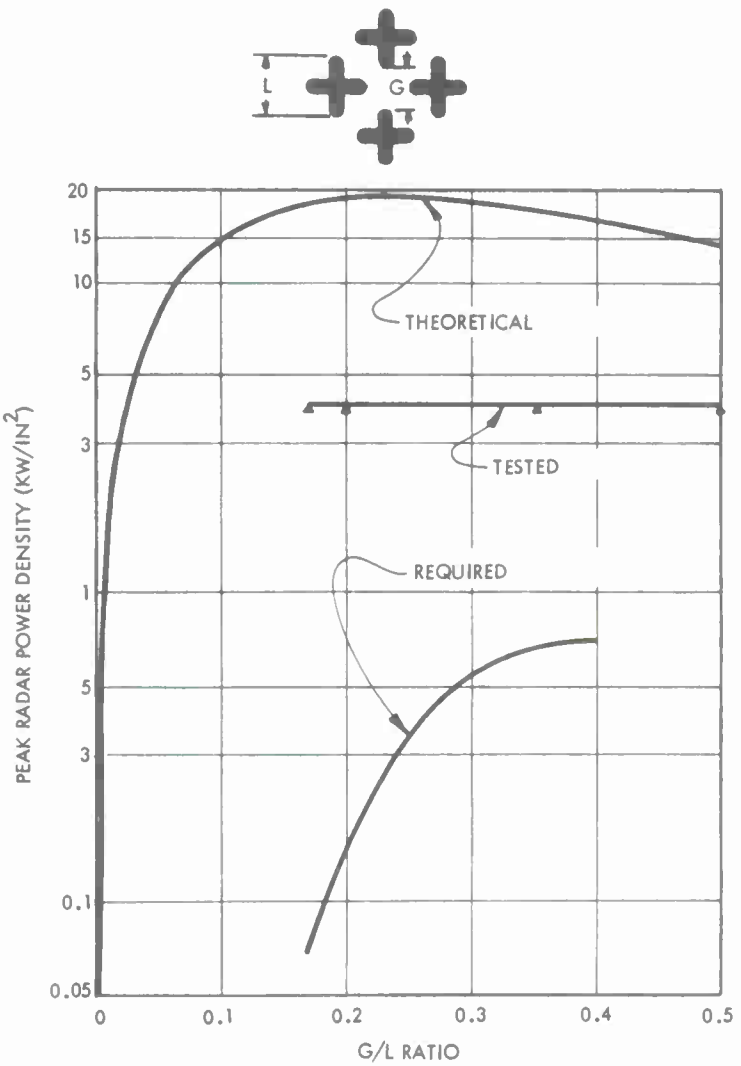

Figure 26 Power Density vs Element Spacing

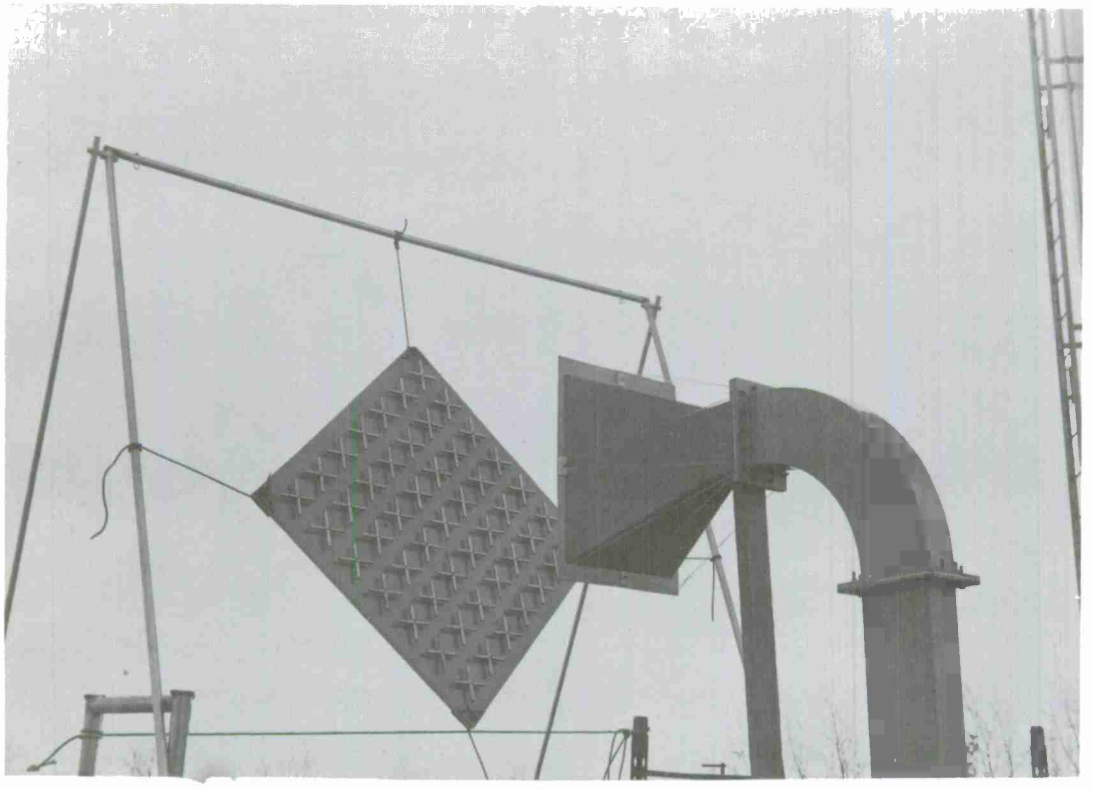

Figure 27 High-Power Test Range

To prevent the possibility of an energy build-up (resonance) in the cavity formed by the FSS subreflector and ground plane, the ground plane was designed to be essentially transparent to L-band while reflective at UHF. This was accomplished by placing a metallic grid formed by 1-inch aluminum strips spaced 7 inches apart on the dielectric ground plane.

The cavity formed by the FSS-radome and ground plane is pressurized with dry nitrogen to exclude water vapor. Since the cavity is a closed structure and a poor dissipator of heat, an external heat exchanger and circulating blower are provided for cavity cooling.

Several controlled power tests were made to determine temperature rise inside the FSS cavity. A cavity temperature rise of 20°F resulted after the FSS was irradiated for one hour at rated power (125 kW average). Table 4 lists the results of these high-power tests.

TABLE 4

M. I. T. HIGH-POWER TEST RESULTS

POWER LEVEL (kW)	TIME MIN.	CAVITY TEMPERATURE °F		AMBIENT °F	
		START	FINISH	START	FINISH
25	30	70	72	73	74
50	30	72	76	74	76
75	50	75	84	78	76
100	60	74.5	92	76	78
100	50	70	83	68	68
125	60	80	102	78	82

CONCLUSIONS

From the reflectivity frequency bandwidth curves plotted in Figures 6 and 7, it is concluded that FSS subreflectors may be designed and fabricated with reflectivity frequency bandwidths greater than 20%, while having a high transmissivity to prime-focus feeds which have a frequency factor spread of 3 or more from the Cassegrainian feed frequency. Peak radar power density capabilities of several kW/in^2 can be incorporated into the FSS design with relative ease. Average power density capabilities of over 100 W/in^2 have been achieved on several test panels.

The upper boundary on the L-band M.I.T.-FSS subreflector loss is taken to be 0.2 dB. The FSS subreflector transmission loss to the prime-focus feeds is deemed negligible. The M.I.T.-FSS subreflector has a power capability well in excess of the required operating levels of 21 W/in^2 average or 700 W/in^2 peak.

REFERENCES

[1] F. O'Nians and J. Matson, "Antenna Feed System Utilizing Polarization Independent Frequency Selective Intermediate Reflector," U. S. Patent 3 231 892, January 25, 1966.

[2] F. O'Nians, "A Frequency Sensitive Cassegrainian Subreflector," Proceedings 14th Annual Antenna Symposium, University of Illinois, October, 1964.

[3] B. A. Munk, "Reflection from Monoplanar Single-Tuned Periodic Surface," ElectroScience Laboratory, Ohio State University, Columbus, Ohio, Report 2382-9, October 14, 1968.

[4] B. A. Munk, "Reflection Properties of Mono- and Bi-Planar Double-Loaded Periodic Surfaces," ElectroScience Laboratory, Ohio State University, Columbus, Ohio, Report 2382-10, October 16, 1968.

[5] R. H. Ott, "Scattering by a Two-Dimensional Periodic Array of Narrow Plates," Radio Science, Vol. 2, No. 11, November, 1967, pp. 1347-1359.

[6] E. P. Irzinski and R. E. Moseley, "A Dichroic Cassegrain Subreflector Utilizing Non-Resonant Elements," Proceedings International Antenna and Propagation Symposium, Washington, D.C., August 1965.

[7] E. C. Jordan, Electromagnetic Waves and Radiating Systems, Englewood Cliffs, N. J.: Prentice-Hall, 1950.

[8] S. A. Schelkunoff and H. T. Friis, Antennas: Theory and Practice, New York: Wiley, 1952.

[9] J. Ruze, private communication.

APPENDIX A

FFS REFLECTIVITY DATA ON FLAT-PANELS

APPENDIX A

FSS REFLECTIVITY DATA ON FLAT-PANELS

Tabulated in Tables A-1 and A-2 is a complete list of the FSS flat-panels which were tested for reflectivity. The key parameters found within the tables are defined in Figure A-1. The measured reflectivity data is plotted in Figures A-3 and A-4 as a function of angle of incidence at f_o for various polarizations. The angle of incidence and the polarization is defined in Figure A-2.

The plotted reflectivity data was taken from over 300 reflectivity patterns. It was this data which formed a solid foundation for the design of the M.I.T.-Millstone Hill FSS Subreflector. In addition, the data is frequency independent in the sense that the plotted responses can be obtained at any frequency f_o by simply scaling the array physical parameters. This implies that a minimal of flat-panel testing would be required for future applications.

Of particular interest are the specific arrays described in Table A-3. Array 03F was used in a full scale subreflector which failed due to the elements being too widely spaced. Arrays 02H, 03H and 07H consist of elements which are scaled (approximately 1/4 scale) to the operational FSS elements. The G/L ratio of the scaled elements varied from 0.15 to 0.50. The 0.2 dB predicted reflectivity loss at the Cassegrainian feed frequency was derived from the reflectivity data of these scaled elements. The average of the two polarizations was used and the power at the various angle of incidences weighed according to their appearance in the actual subreflector in conjunction with the power density along the subreflector. Arrays 04H, 05H and 06H consist of full scale elements varying from a G/L ratio of 0.20 to 0.50. The G/L ratio of the elements in the operational subreflector varied somewhat linearly from a G/L ratio of 0.4 at the subreflector center to 0.17 at the subreflector edge.

TABLE A-1

FSS DATA ON FLAT ELEMENT ARRAYS

ARRAY	01F*	02F	03F**	04F	05F	06F	07F	08F
G/L	0.19	0.74	0.73	0.32	0.20	0.35	0.50	0.35
W/L	0.110	0.118	0.116	0.127	0.132	0.132	0.132	0.116
L(in)	2.375	1.487	4.860	1.375	1.186	1.186	0.186	4.860
G(in)	0.451	1.100	3.548	0.440	0.237	0.415	0.593	1.701
S(in)	2.826	2.588	8.408	1.815	1.423	1.601	1.779	6.561
a(in)	1.998	1.829	5.944	1.283	1.006	1.132	1.257	4.638
W(in)	0.260	0.175	0.562	0.175	0.156	0.156	0.156	0.562
t	0.002	0.040	0.125	0.040	0.015	0.015	0.015	0.015
f_o(GHz)	2.2	4.1	1.295	4.1	5.8	5.8	5.8	1.4
λ_o(in)	5.36	2.88	9.11	2.88	2.03	2.03	2.03	8.43
G/λ_o	0.084	0.382	0.390	0.153	0.117	0.204	0.291	0.202
a/λ_o	0.372	0.636	0.652	0.446	0.495	0.556	0.618	0.550
W/λ_o	0.048	0.061	0.062	0.061	0.077	0.077	0.077	0.067
L/λ_o	0.443	0.516	0.533	0.478	0.583	0.583	0.583	0.577
N	15X15	13X13	7X7	18X18	15X15	15X15	15X15	7X7
SF	1.70	3.17	1.00	3.17	4.48	4.48	4.48	1.08
GF(in)	0.77	3.48	3.55	1.39	1.06	1.86	2.66	1.84

f_o Nominal frequency in GHz

λ_o Nominal wavelength in inches

N Number of rows by number of columns in array

SF Scale factor relative to M.I.T. center frequency

GF Full scale gap when scaled to f_o

*Dielectric Embedded Cross-Dipoles

**M.I.T. #1 GRID PATTERN

TABLE A-2

FSS DATA ON CYLINDRICAL ELEMENT ARRAYS

ARRAY	01H	02H*	03H*	04H**	05H**	06H**	07H*
G/L	0.35	0.35	0.50	0.20	0.35	0.50	0.15
W/L	0.132	0.111	0.111	0.108	0.108	0.108	0.111
L(in)	1.186	1.406	1.406	5.211	5.211	5.211	1.406
G(in)	0.415	0.492	0.703	1.042	1.824	2.605	0.211
S(in)	1.601	1.898	2.109	6.253	7.035	7.816	1.617
a(in)	1.132	1.342	1.491	4.421	4.974	5.526	1.143
D(in)	0.156	0.156	0.156	0.562	0.562	0.562	0.156
f_o	5.8	4.8	4.8	1.295	1.295	1.295	4.8
λ_o	2.03	2.46	2.46	9.11	9.11	9.11	2.46
G/λ_o	0.204	0.200	0.286	0.114	0.200	0.286	0.086
a/λ_o	0.556	0.546	0.606	0.485	0.546	0.606	0.465
W/λ_o	0.077	0.063	0.063	0.062	0.062	0.062	0.063
L/λ_o	0.583	0.572	0.572	0.572	0.572	0.572	0.572
N	15X15	15X15	15X15	7X7	7X7	7X7	15X15
SF	4.48	3.71	3.71	1.00	1.00	1.00	3.71
GF(in)	1.86	1.82	2.61	1.042	1.824	2.605	0.782

f_o Nominal frequency in GHz

λ_o Nominal wavelength in inches

N Number of rows by number of columns in array

SF Scale factor relative to M.I.T. center frequency

GF Full scale gap when scaled to f_o

* M.I.T. #2 Scaled Elements

** M.I.T. #2 Full Scale Elements

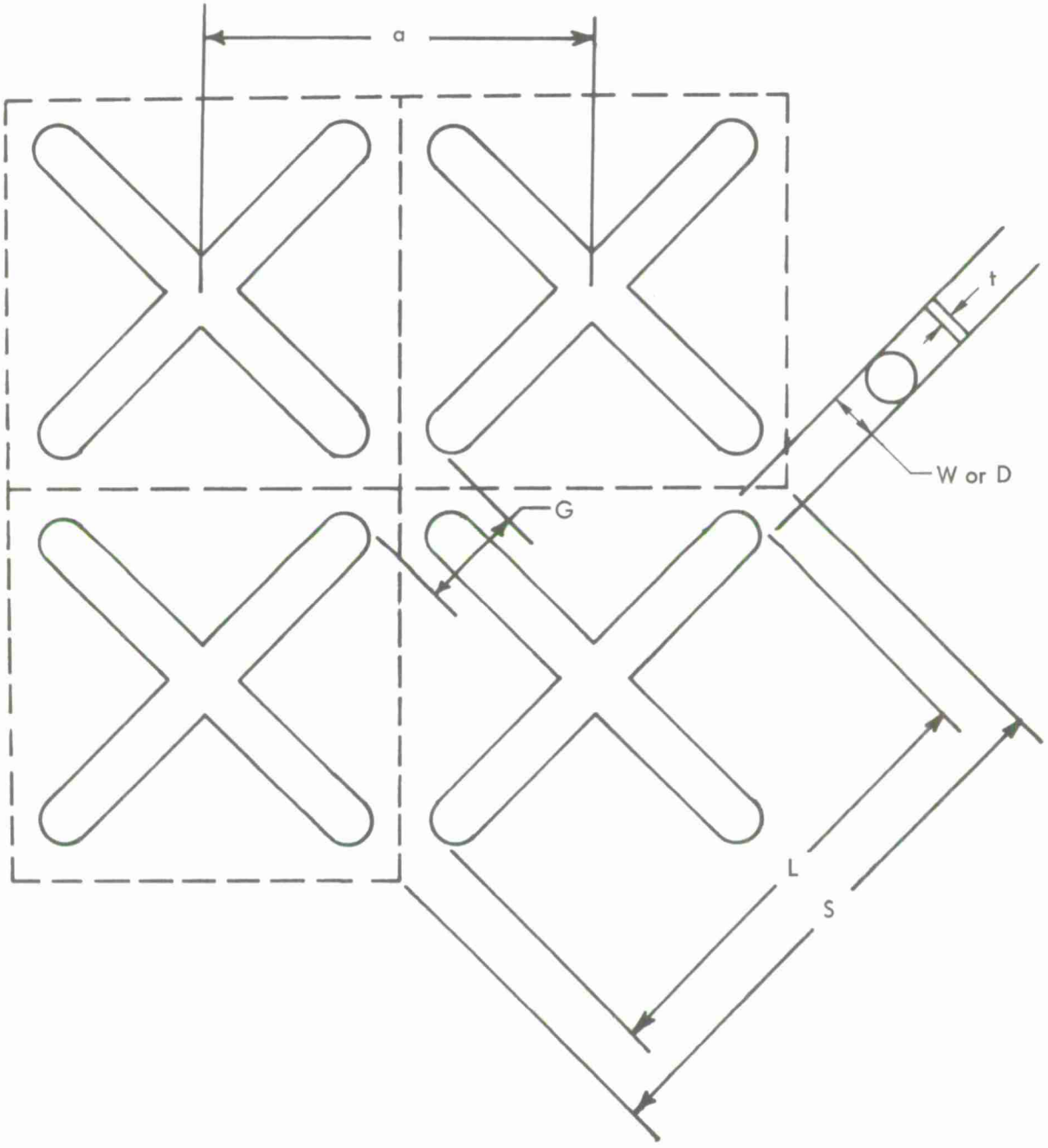

Figure A-1 Array Geometry

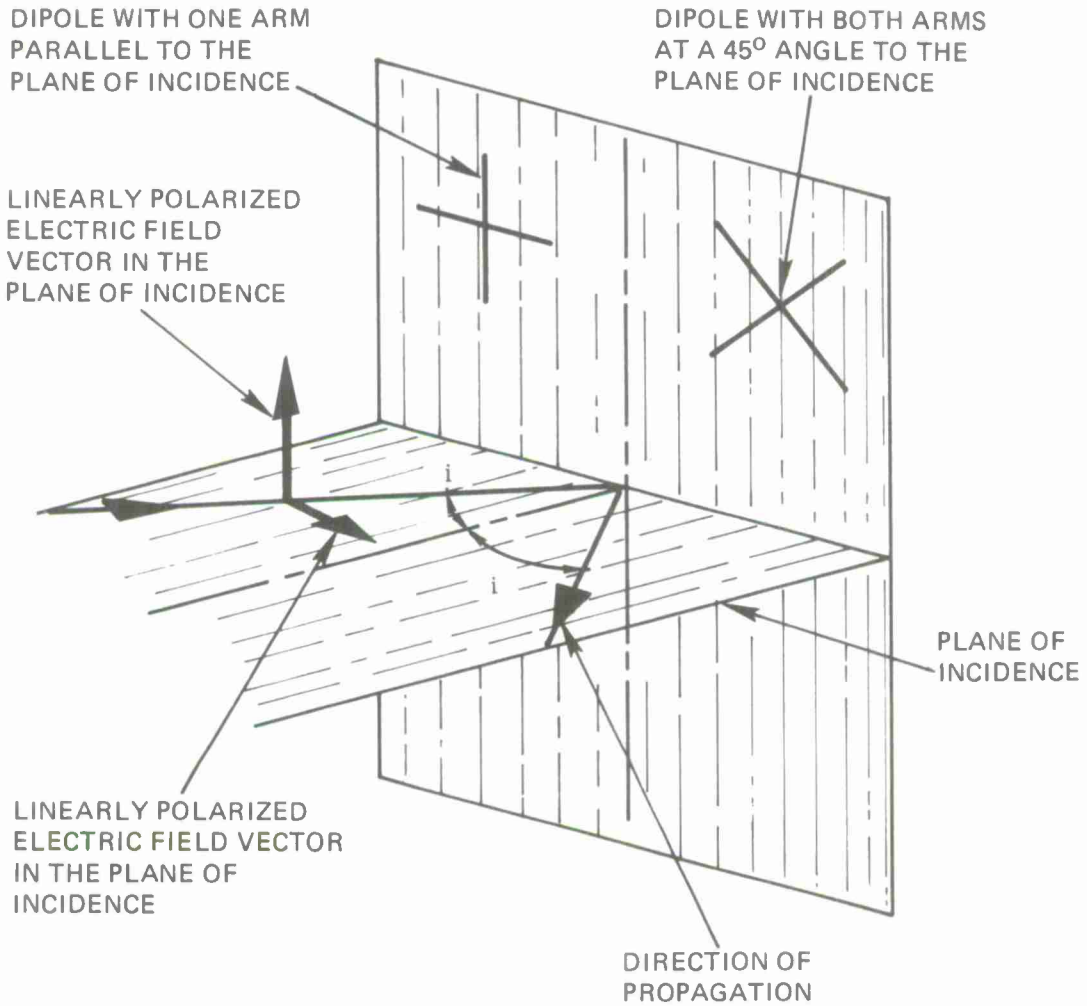

i = Angle of Incidence = Angle of Reflection

Figure A-2 Nomenclature

x↑ Represents a linearly polarized electric field perpendicular to the plane of incidence with the crossed dipole arms at a 45° angle to the plane of incidence.

+↑ Represents a linearly polarized electric field perpendicular to the plane of incidence wiht one crossed dipole arm parallel to the plane of incidence.

x→ Represents a linearly polarized electric field parallel to the plane of incidence with the crossed dipole arm at a 45° angle to the plane of incidence.

+→ Represents a linearly polarized electric field parallel to the plane of incidence with one crossed dipole arm parallel to the plane of incidence.

x↻ Represents a circularly polarized electric field with the crossed dipole arms at a 45° angle to the plane of incidence.

+↻ Represents a circularly polarized electric field with one crossed dipole arm parallel to the plane of incidence.

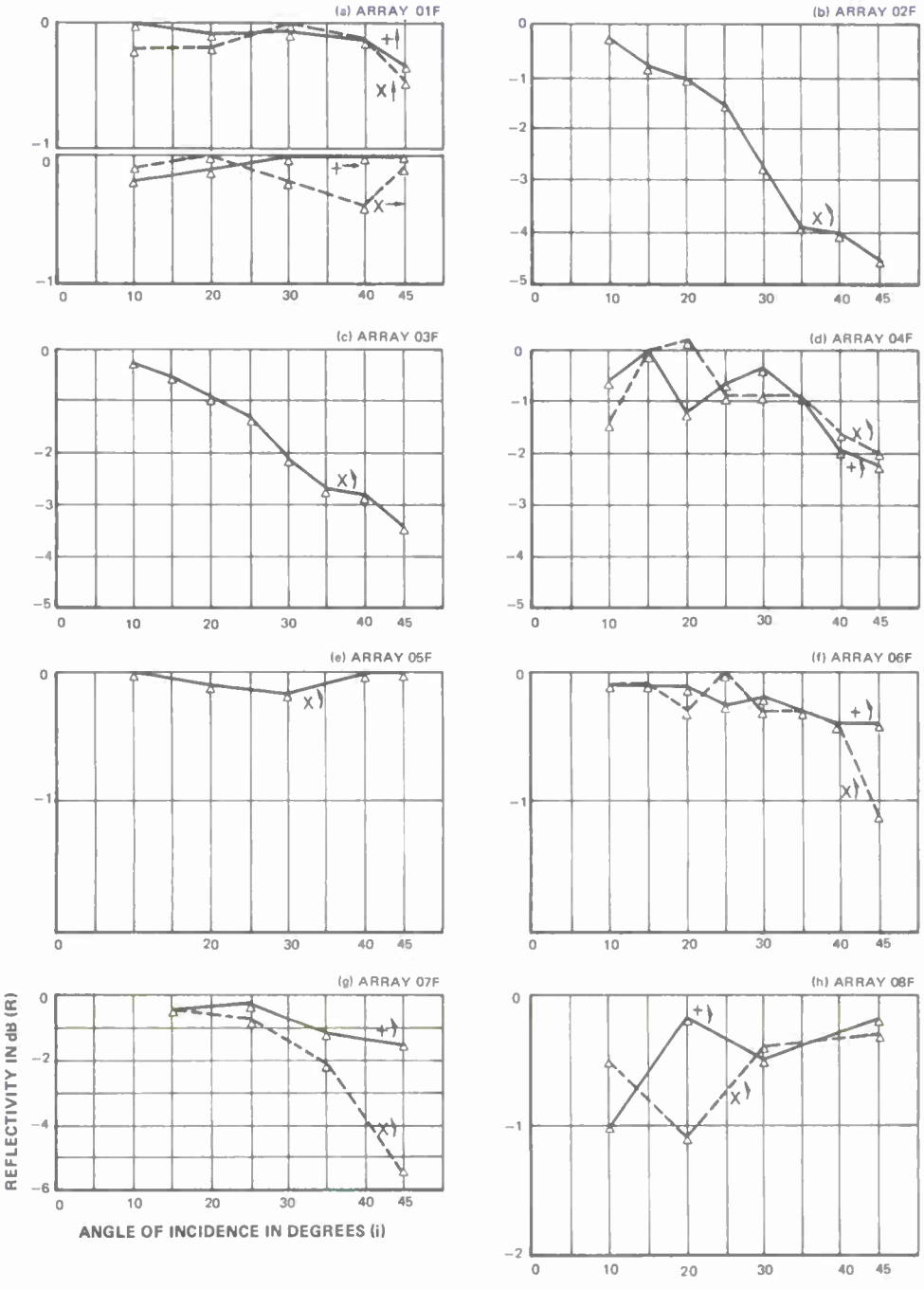

Figure A-3 Reflectivity as a Function of Angle of Incidence for Flat-Element Arrays

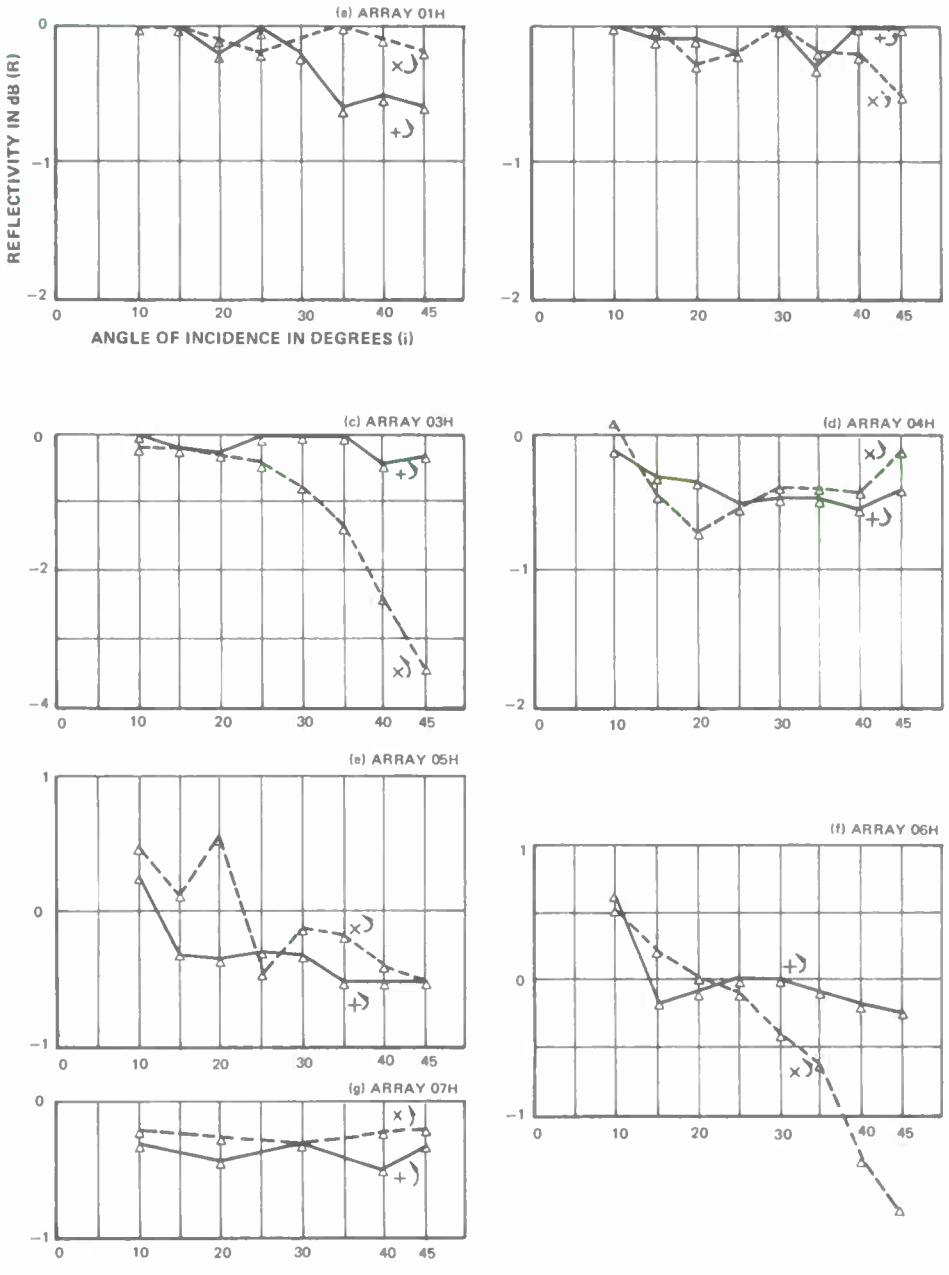

Figure A-4 Reflectivity as a Function of Angle of Incidence for Cylindrical Element Arrays

TABLE A-3

FSS ARRAYS OF PARTICULAR INTEREST

APPLICATION	ARRAY	G/L
M.I.T. FSS #1 (Full Scale Elements and Grid Pattern of an FSS Which Failed)	03H	0.73
M.I.T. FSS #2 (Scaled Elements of Operational FSS)	02H 03H 07H	0.35 0.50 0.15
M.I.T. FSS #2 (Full Scale Elements of Operational FSS)	04H 05H 06H	0.20 0.35 0.50

APPENDIX B

FSS HEATING - NEAR FIELD OF ARRAYS

APPENDIX B

FSS HEATING – NEAR FIELD OF ARRAYS

Initial calculations, which assumed that the subreflector array of crosses with 0.5 inch standoffs behaved as a solid metal subreflector, resulted in an estimated radome surface temperature increase at the outer dielectric surface of 22°F and 38.4°F at the inner surface at rated power. This calculation assumed that only the outer dielectric skin dissipated the heat energy. In the high power tests both surfaces are exposed to ambient air and the temperature rise should be only 11°F at rated or nominal power. Subsequent high power tests indicated surface temperature rises as high as 150°F at power levels slightly above rated power.

As the thermal analysis was based on the assumption that the dipole layer could be replaced by a metallic sheet, it was decided to explore the near field of a dipole array as an attempt to dissolve the temperature discrepancies.

By combining the near field expressions given by King [B.1] for a half-wave dipole carrying a sinusoidal current with an appropriate incident field, the net power density close to the array could be determined. To approximate the actual situation as closely as possible, the following conditions were imposed:

- Half-wavelength dipoles were used in a large array.
- The array was inter-leaved in the y-z plane, as shown in Figure B-1.
- A plane wave incident field was included and its magnitude adjusted to create a standing wave in front or little radiation behind the array

The original King equations were converted from cylindrical to rectangular coordinates. Then the various contributions from the dipole locations on the square array were summed in phase and magnitude with the magnitude adjusted incident field at a general point in front or back of the array.

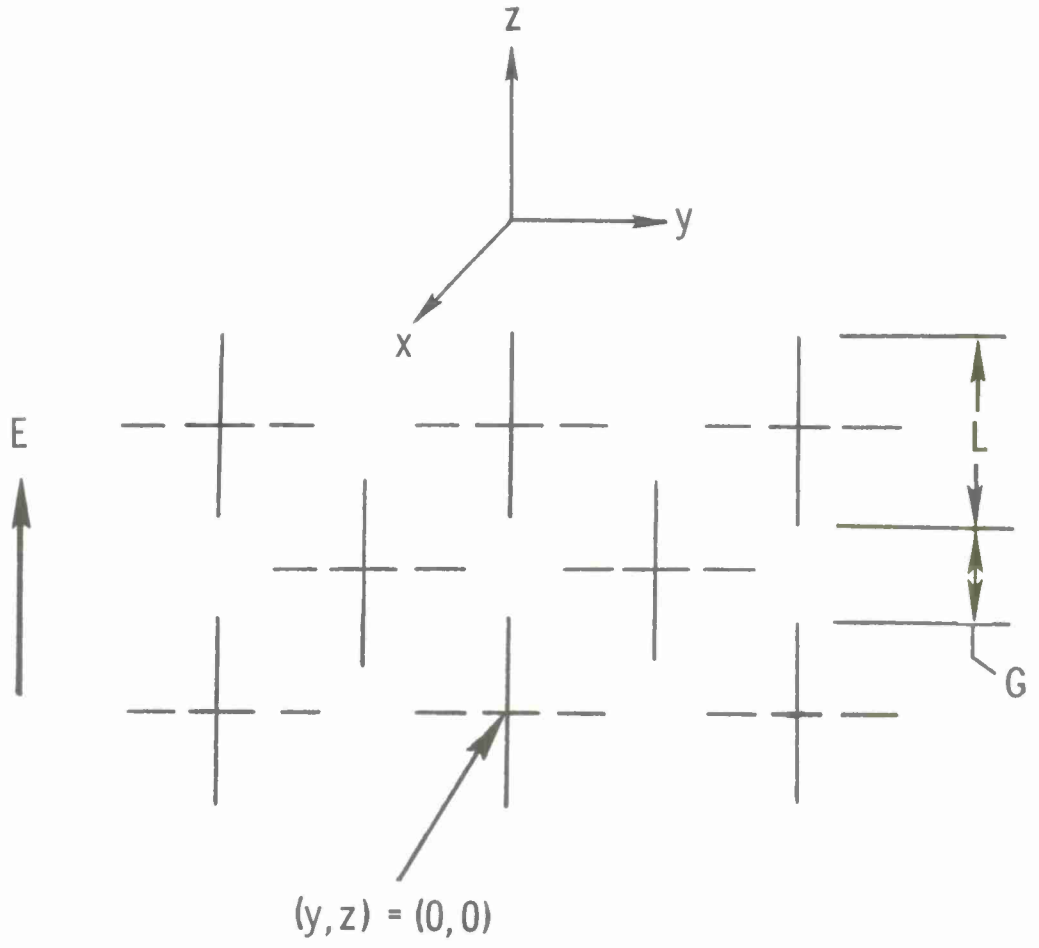

Figure B-1 Array Geometry

Plotted in Figure B-2 is the calculated total power density in a plane perpendicular to the array, (x-z plane) but containing the dipole elements (y = 0) for $(G + L)/\lambda = 0.7$. Figure B-3 is for a displace plane ($y = 0.125\lambda$). The field is calculated for various values of "z", where "z" is in wavelengths.

Several aspects of these curves are noteworthy, namely:

- In front of the array a standing wave pattern occurs and the power density at a quarter-wavelength is closely four times that of the incident wave everywhere, even between the dipoles. Beyond a quarter-wavelength, it would be difficult for an explorer to tell whether he is in the presence of a metallic plate or a dipole array.
- The curves "z" = 0 (array axis) and "z" = 0.35 (between dipole rows) represent lines of symmetry where certain rectangular components vanish and the near near-field is therefore small.
- The field achieves high values near the ends of the dipoles in the plane containing the dipoles. For this array the power density is 13 times the incident field at a distance of 0.05 wavelenghts (0.45").
- The near near-field behind the array is identical to that in the front, so that there would be no advantage in mounting dipoles close to the front of the substrate.
- At distances greater than quarter-wave behind the array, the field is low everywhere, at least 16 dB below the front field maximum.

Plotted in Figure B-4 are curves similar to those plotted in Figure B-3, except that it is for a less dense array, $(G+L)/\lambda = 0.862$. The behavior of the less dense array is similar to that of the denser array, except that the near near-field is about 3 dB higher. It appears that dense arrays have a tendency to cancel the near near-field components to a greater degree than less dense arrays.

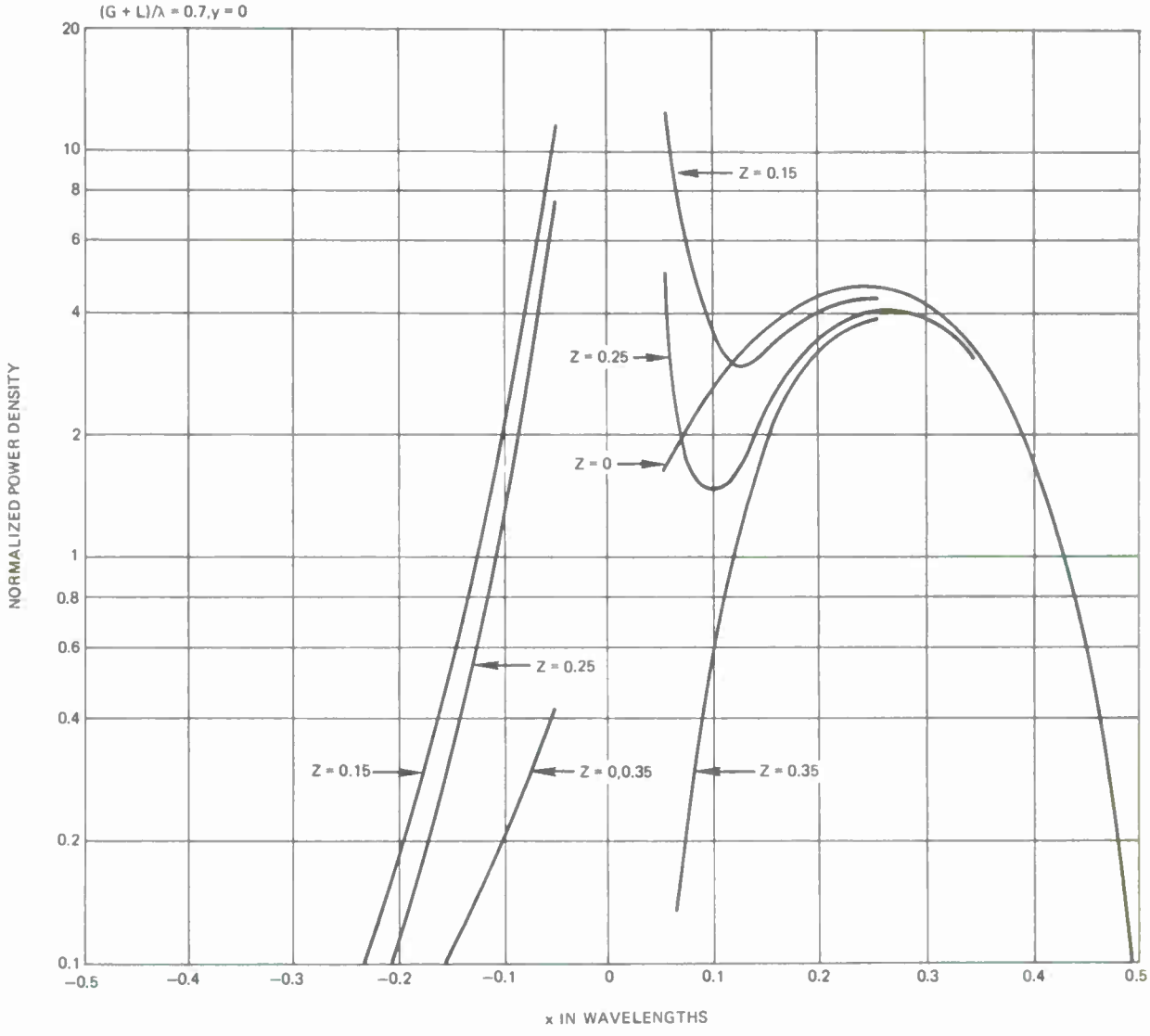

Figure B-2 Power Density vs x

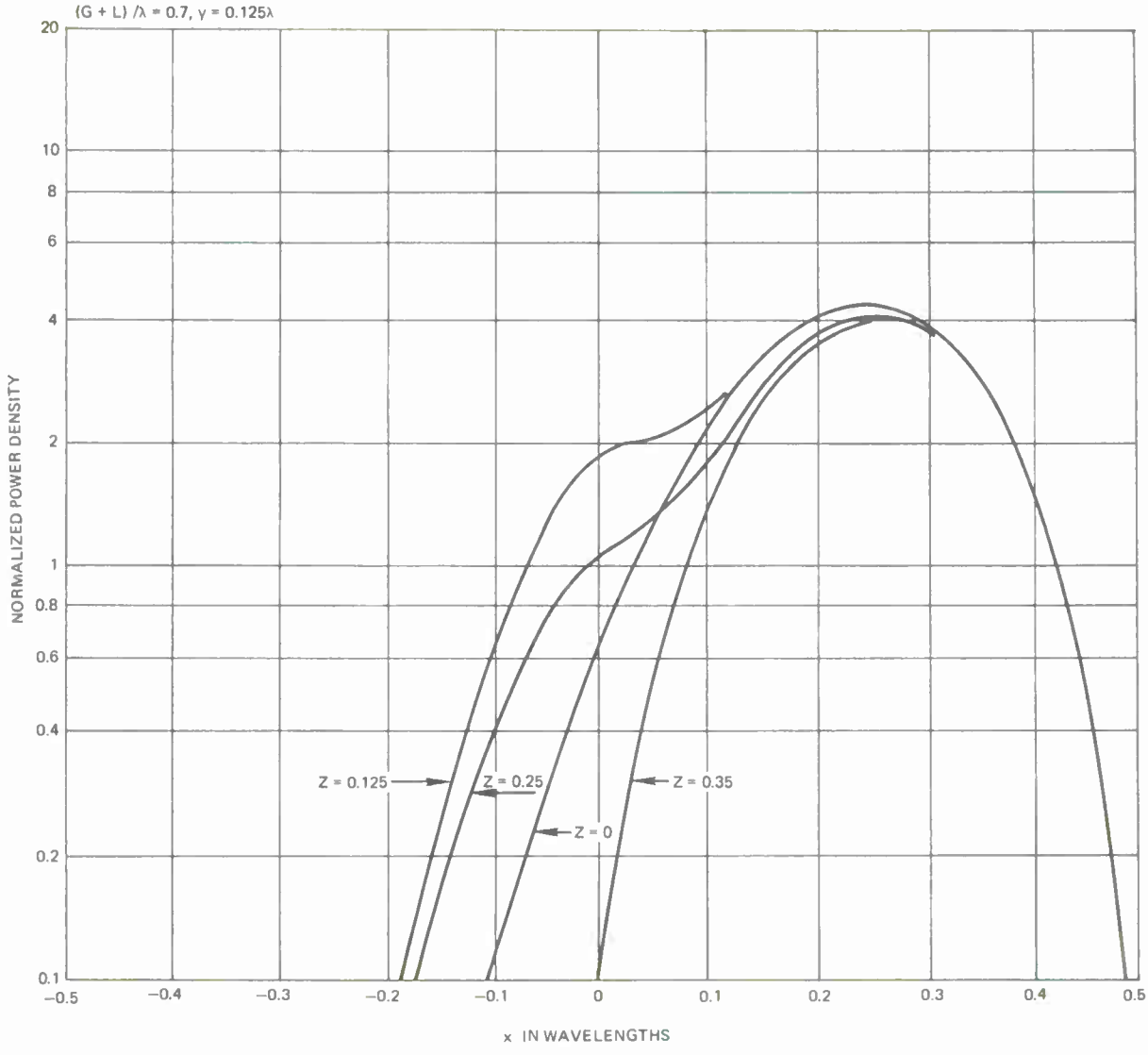

Figure B-3 Power Density vs x

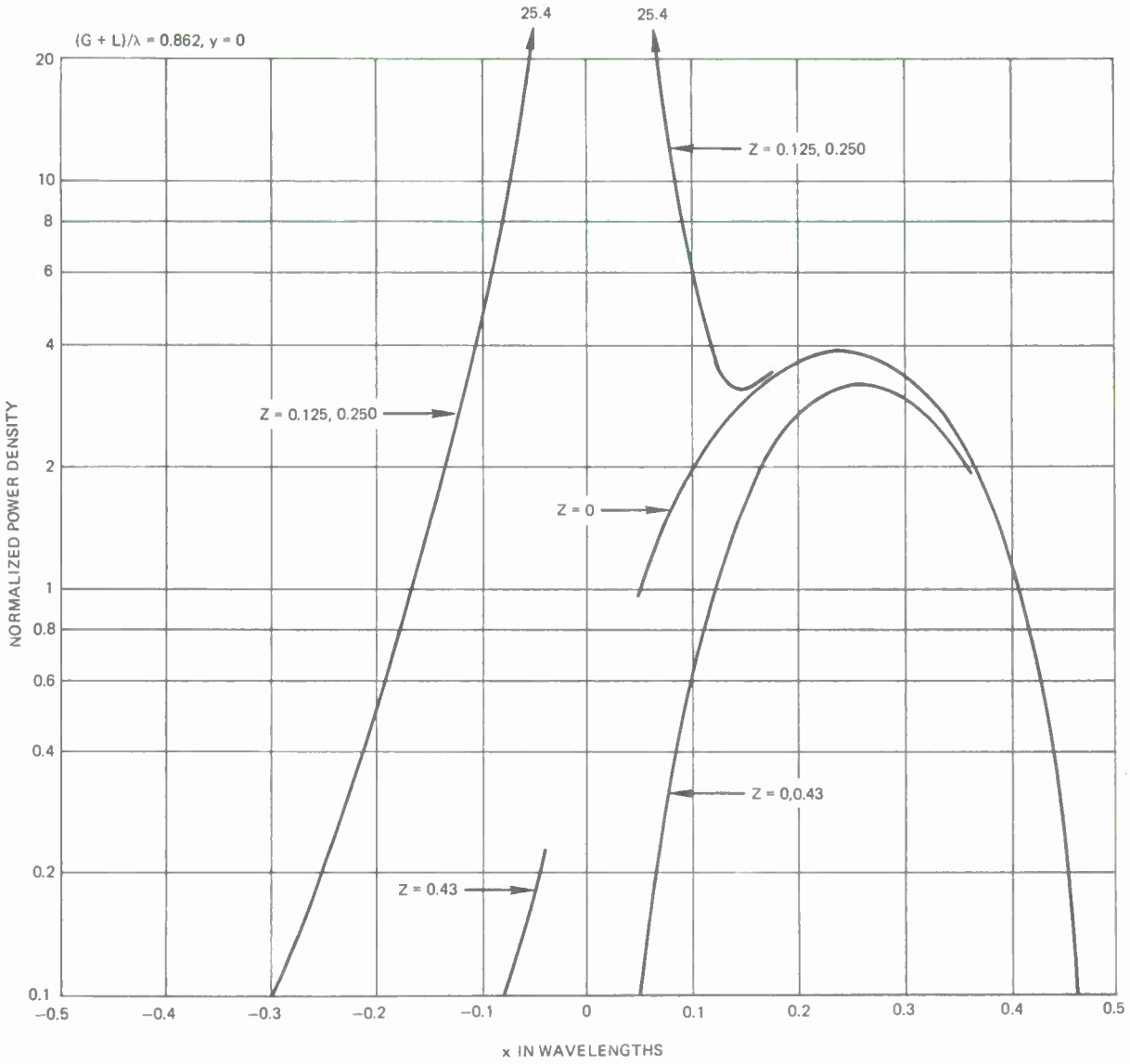

Figure B-4 Power Density vs x

Tabulated in Table B-1 are the calculated peak power densities relative to the incident field at a 0.05 wavelength standoff distance (0.45 inches) for the previously mentioned element spacings. Notice from this table that the relative power density is over 25 times greater than the incident power density at spacings corresponding to the center of the subreflector.

The theoretical power density is quite small at a half-wavelength spacing, as evidenced by Figures B-2 to B-4. For this reason, half-wavelength standoffs were eventually selected for the M.I.T.-FSS.

TABLE B-1

PEAK POWER DENSITY AT 0.05 WAVELENGTHS (0.45 INCHES)

ARRAY DENSITY $[(G+L)/\lambda]$	RELATIONSHIP TO M.I.T.-SUBREFLECTOR	RELATIVE POWER DENSITY TO INCIDENT POWER
0.7	approximately the M.I.T.-FSS Outer Spacing	13.0
0.862	approximately the M.I.T.-FSS Center Spacing	25.4

REFERENCES

[B.1] R. W. King, The Theory of Linear Antennas, Cambridge, Mass.: Harvard Press, p. 528.

APPENDIX C
FULL-SCALE SECONDARY PERFORMANCE

APPENDIX C

FULL-SCALE SECONDARY PERFORMANCE

Preliminary on-site radio star measurements and radiation patterns have been recorded on the Millstone Hill Antenna with the FSS subreflector installed. This data is presented in Table C-1 and Figures C-1 through C-4.

It is felt that the 0.5 dB difference in gain between the metal and FSS #2 subreflector cases, as measured by the radio star technique, is not an FSS loss, but is due rather to measurement accuracy or subreflector alignment differences.

TABLE C-1

L-BAND SECONDARY PERFORMANCE SUMMARY

	Metal Subreflector (7/69)	FSS #1* Subreflector (2/2/70)	FSS #2 Subreflector (5/29/70)
Gain from Cass. A	47.2 dB	43.8 dB	46.7 dB
Efficiency	44%	22%	40%
3 dB Bandwidth EL	0.596°	0.649°	0.610°
3 dB Bandwidth AZ	0.606°	0.685°	0.602°

* (Original FSS which consequently failed when exposed to high power)

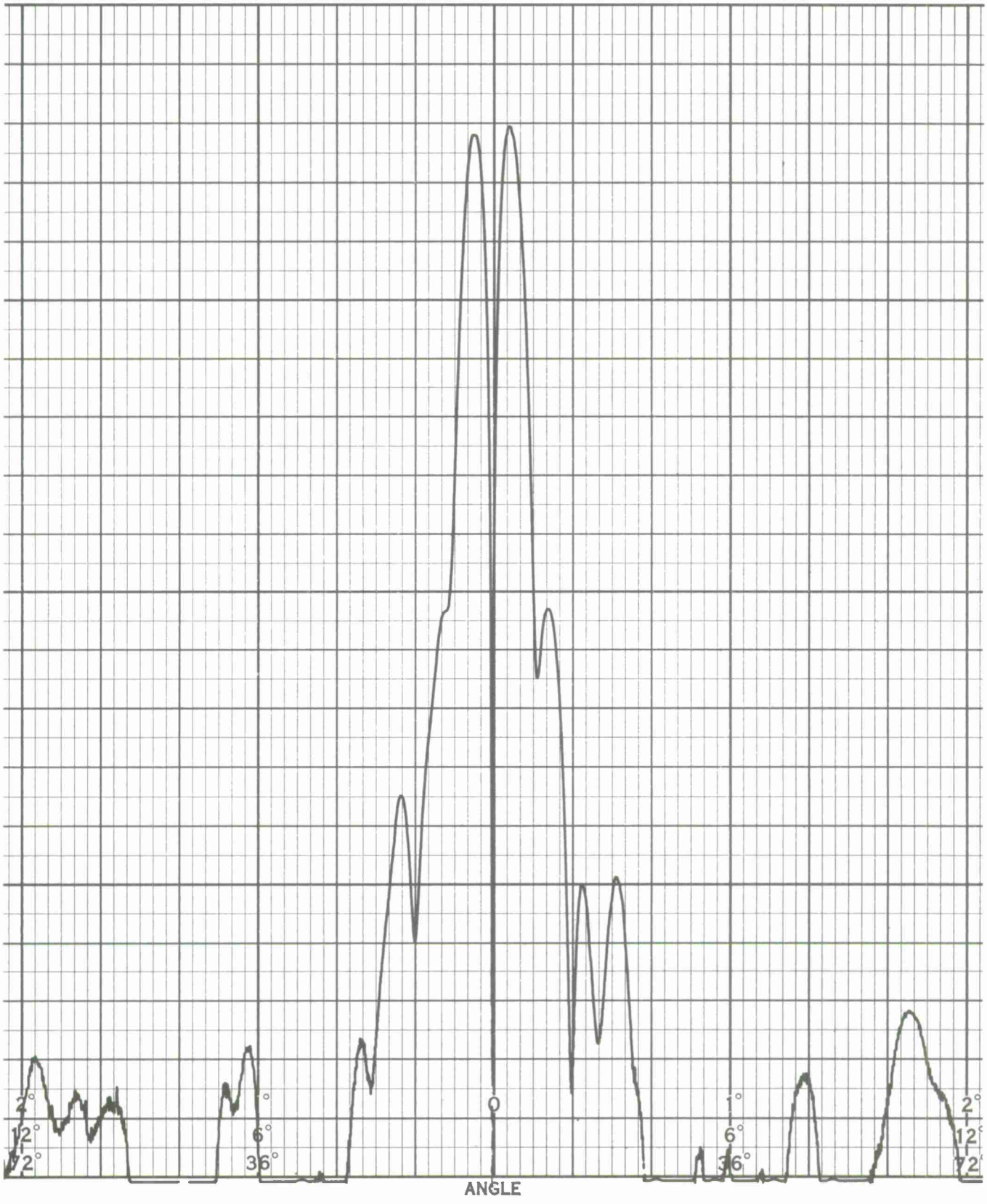

Figure C-1(a) Full Scale L-Band Secondary Difference Patterns at 1295 MHz with FSS No. 2, AZ Scan, Transmit Source - Vertical Polarization, Receive - RHCP.

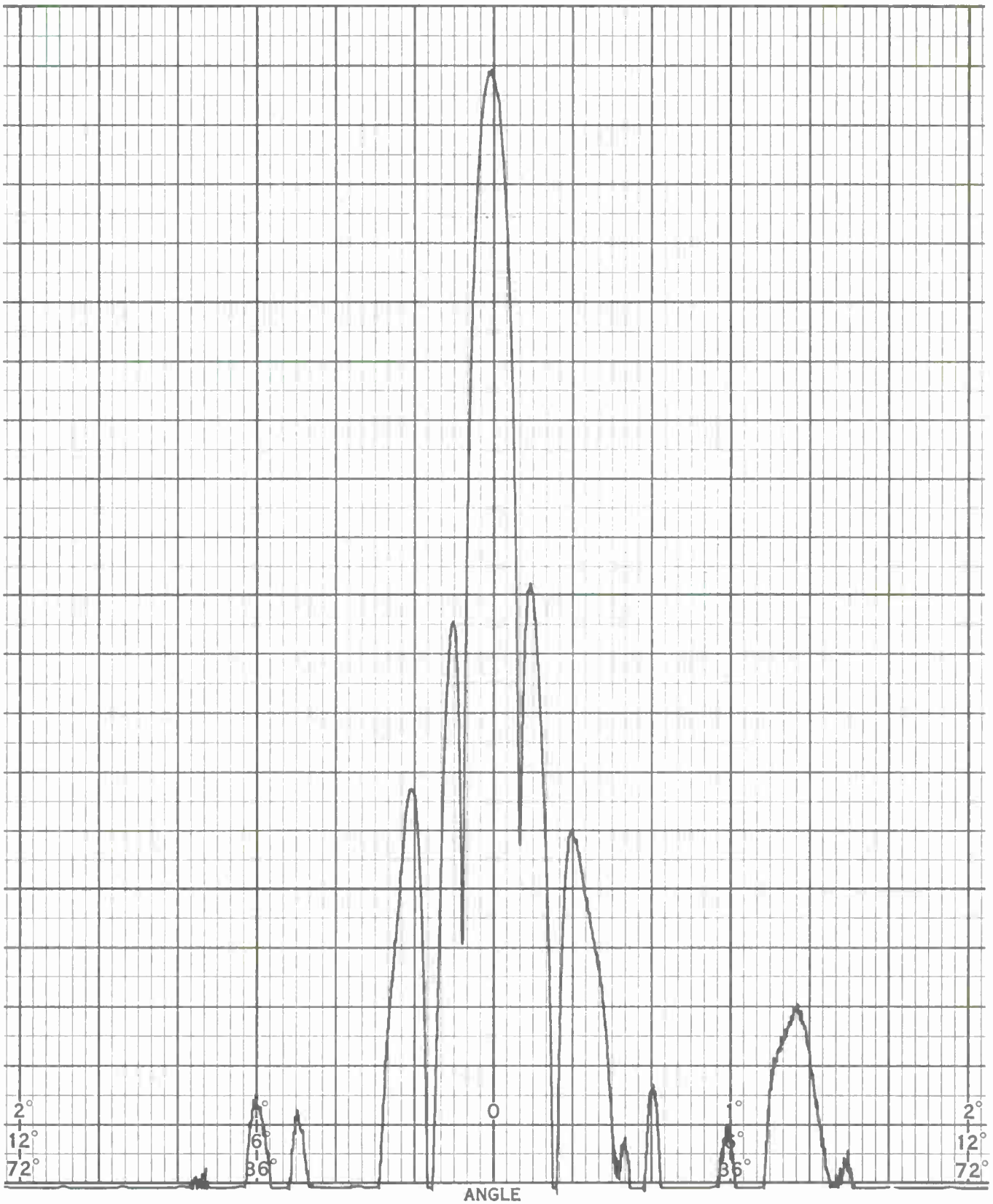

Figure C-1(b) Full Scale L-Band Sum Patterns at 1295 MHz with FSS No. 2, AZ Scan, Transmit Source - Vertical Polarization, Receive-RHCP.

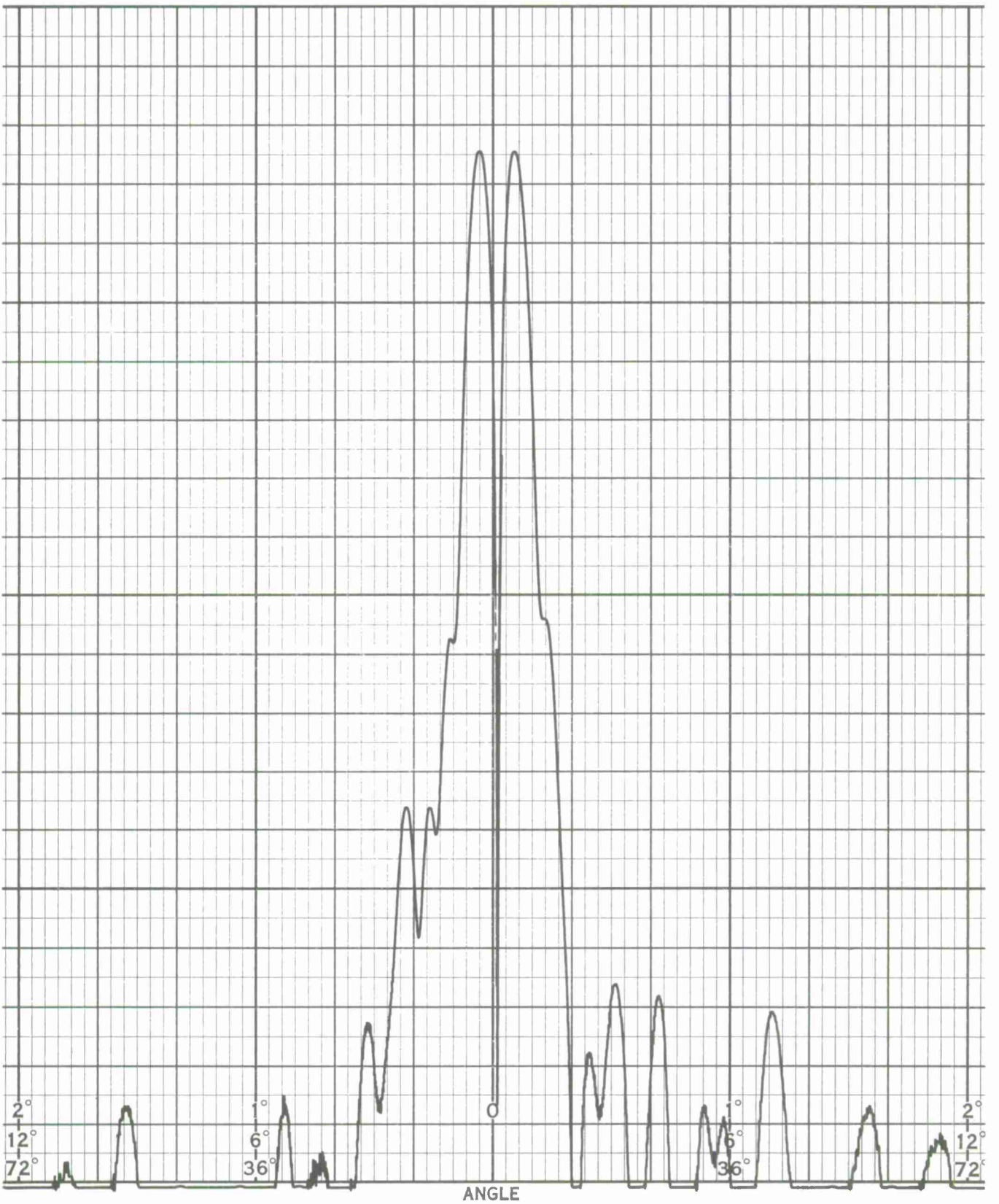

Figure C-2(a) Full Scale L-Band Secondary Difference Patterns at 1295 MHz with FSS No. 2, AZ Scan, Transmit Source - Horizontal Polarization, Receive - RHCP.

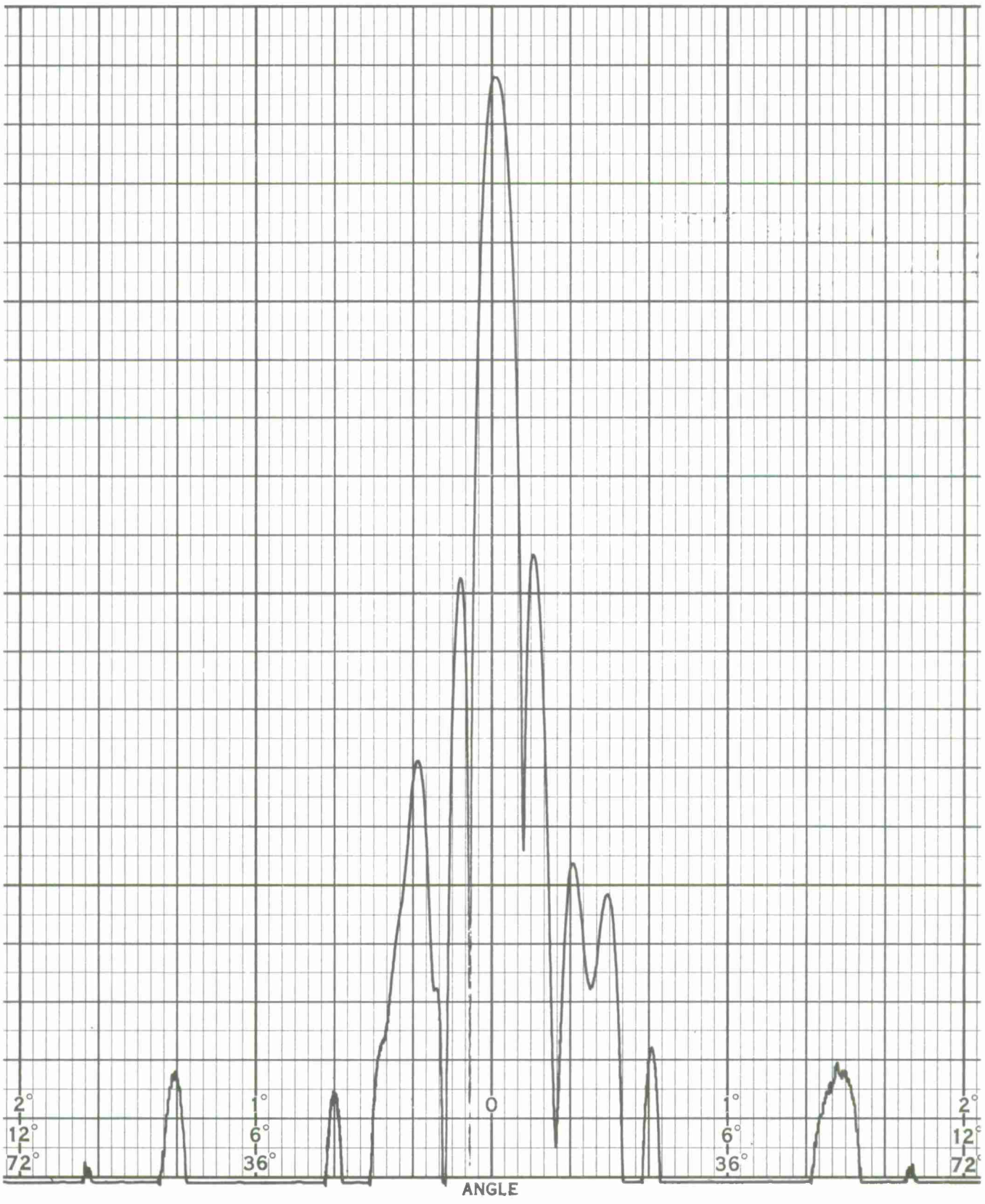

Figure C-2(b) Full Scale L-Band Sum Patterns at 1295 MHz with FSS No. 2, AZ Scan, Transmit Source - Horizontal Polarization, Receive-RHCP.

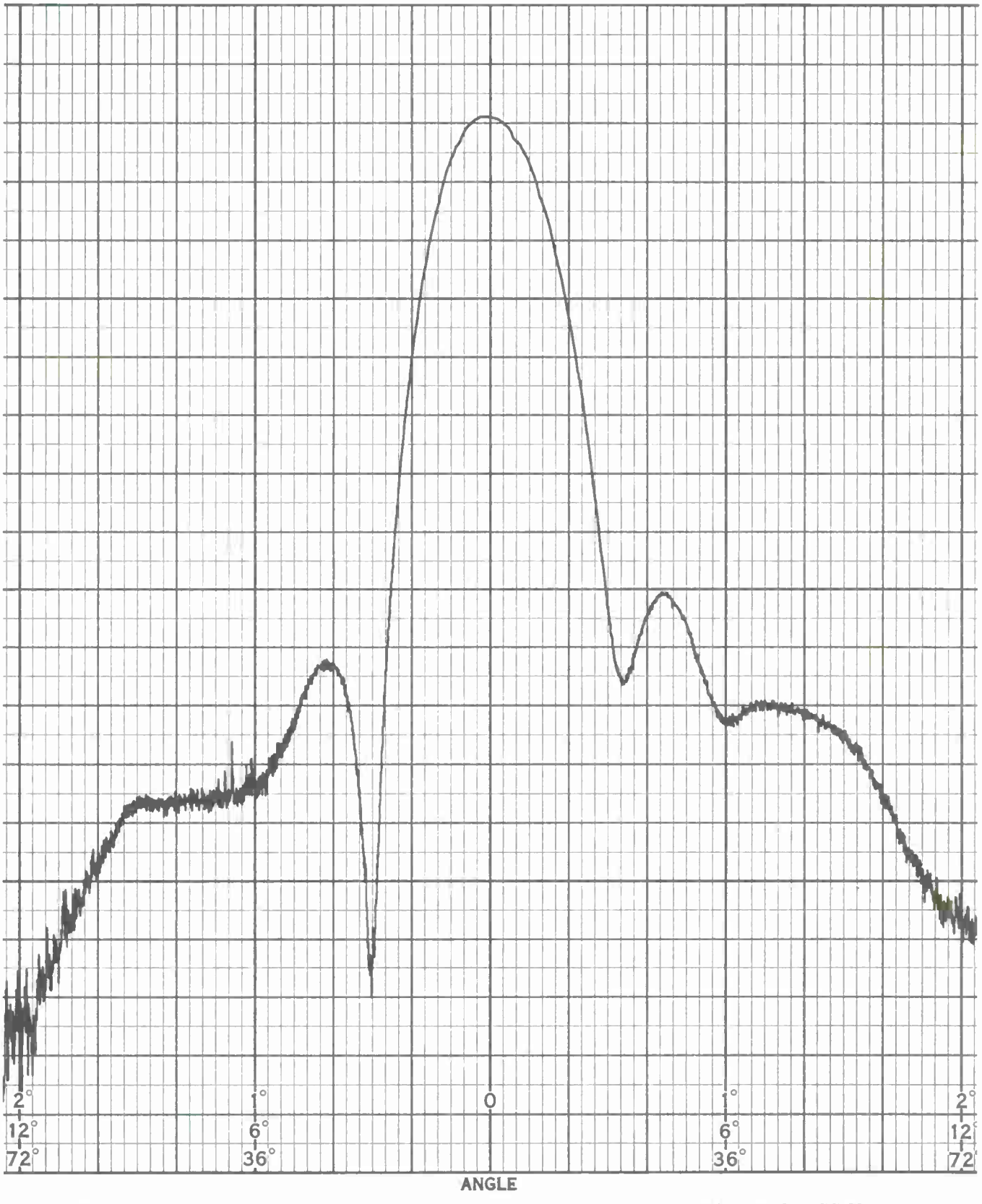

Figure C-3 Full Scale UHF Secondary Sum Patterns at 395 MHz with FSS No. 2
AZ Scan, Transmit Source- RHCP, Receive - RHCP

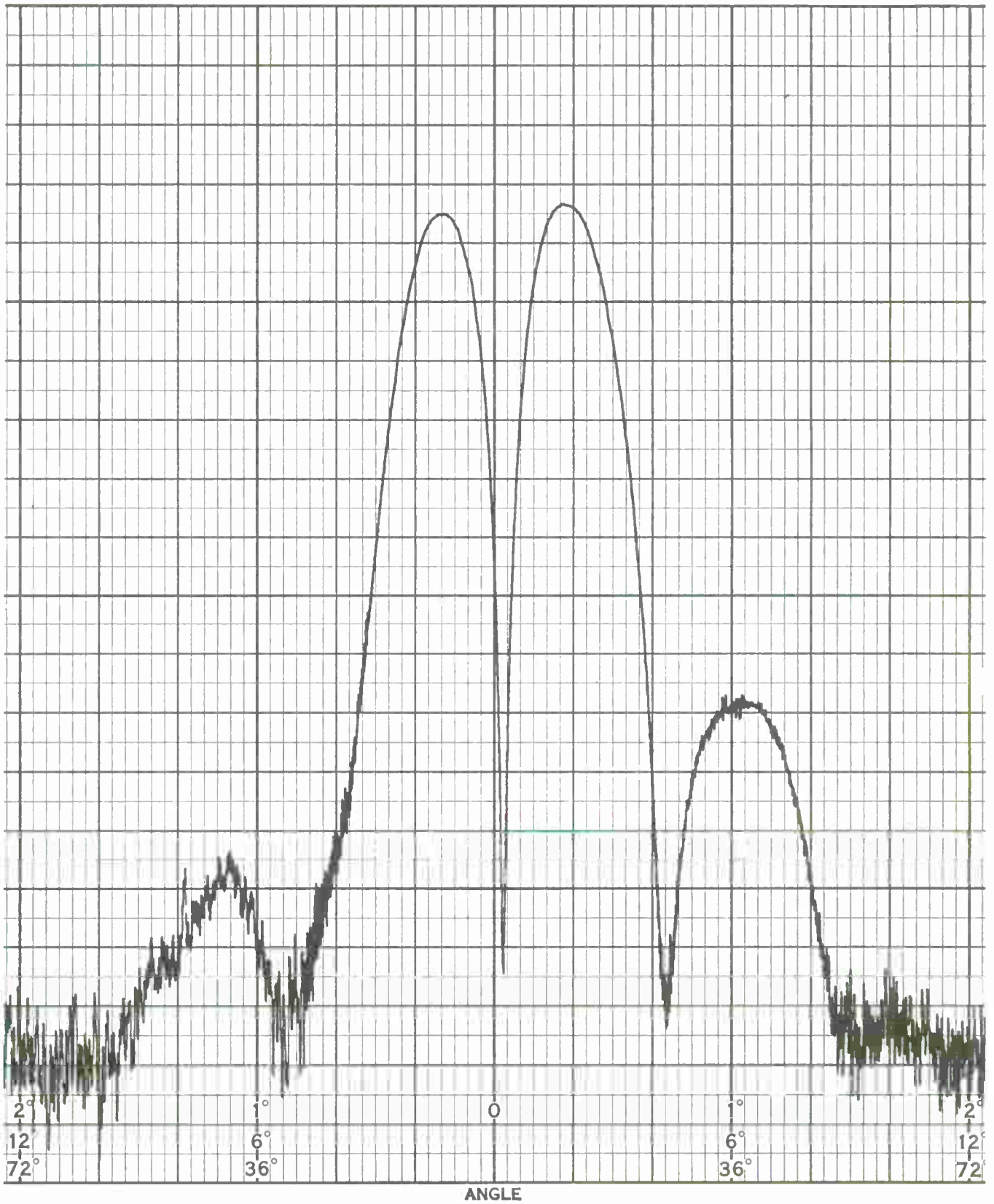

Figure C-4 Full Scale UHF Secondary Difference Patterns at 395 MHz with FSS No. 2, AZ Scan, Transmit Source - RHCP, Receive - RHCP.

ACKNOWLEDGEMENT

This technical report summarizes the results of a coordinated effort performed by the M. I. T. Lincoln Laboratory and the Philco-Ford Corporation WDL.

We wish to express our appreciation specifically to Mr. M. L. Stone and Dr. J. Ruze of the M. I. T. Lincoln Laboratory. The former for providing the high-power test data and the latter for his technical guidance. To Mr. A. A. Gradisar of the Philco-Ford Corporation WDL, we would like to extend our special gratitude for his contributions on the electro-mechanical design efforts, and to Mr. G. H. Schennum for preparing this report as well as contributing to the electrical design.

UNCLASSIFIED
Security Classification

DOCUMENT CONTROL DATA – R&D

(Security classification of title, body of abstract and indexing annotation must be entered when the overall report is classified)

1. ORIGINATING ACTIVITY *(Corporate author)*
Philco-Ford Corporation
under Purchase Order to M.I.T. Lincoln Laboratory

2a. REPORT SECURITY CLASSIFICATION
Unclassified

2b. GROUP
None

3. REPORT TITLE
Frequency Selective Surface Subreflector Development Report
(29 January 1969 to 30 May 1970)

4. DESCRIPTIVE NOTES *(Type of report and inclusive dates)*
Documents FSS Subreflector Developed for the M.I.T. - Millstone Hill Antenna

5. AUTHOR(S) *(Last name, first name, initial)*
Schennum, Gary H.

6. REPORT DATE	7a. TOTAL NO. OF PAGES	7b. NO. OF REFS
2 November 1970	47	10

8a. CONTRACT OR GRANT NO.
AF19(628)-5167
b. PROJECT NO.
7X263304D215
c.
d. Purchase Order No. A-5137

9a. ORIGINATOR'S REPORT NUMBER(S)
WDL-TR4327

9b. OTHER REPORT NO(S) *(Any other numbers that may be assigned this report)*
ESD-TR-70-418

10. AVAILABILITY/LIMITATION NOTICES
This document has been approved for public release and sale;
its distribution is unlimited.

11. SUPPLEMENTARY NOTES
None

12. SPONSORING MILITARY ACTIVITY
Office of the Chief of Research & Development, Department of the Army

13. ABSTRACT
This development report describes the Frequency Selective Surface Subreflector developed for the M.I.T. Lincoln Laboratory-Millstone Hill Field Station. Before specifically describing the M.I.T.-FSS reflector, general design information applicable to any FSS reflector is given in the early parts of the text. A later section, which is titled "Application in the Final Assembly", describes the M.I.T.-FSS in particular. Back-up data used in the M.I.T.-FSS design is given in the Appendices.

14. KEY WORDS
Cassegrainian Radar Antenna
Frequency Selective Subreflector

UNCLASSIFIED
Security Classification

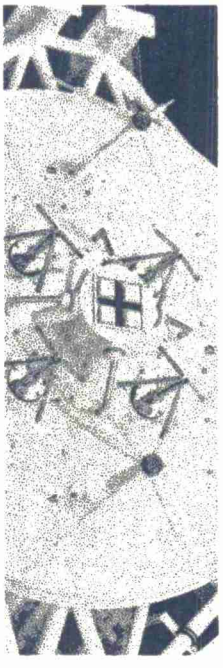

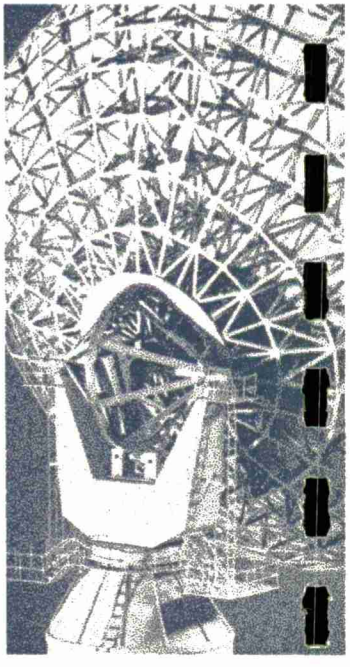

PHILCO Ford

WDL DIVISION
Philco-Ford Corporation
3939 Fabian Way
Palo Alto, California 94303